Neuron

NeuroResource

Single-neuron projectomes of mouse paraventricular hypothalamic nucleus oxytocin neurons reveal mutually exclusive projection patterns

Graphical abstract

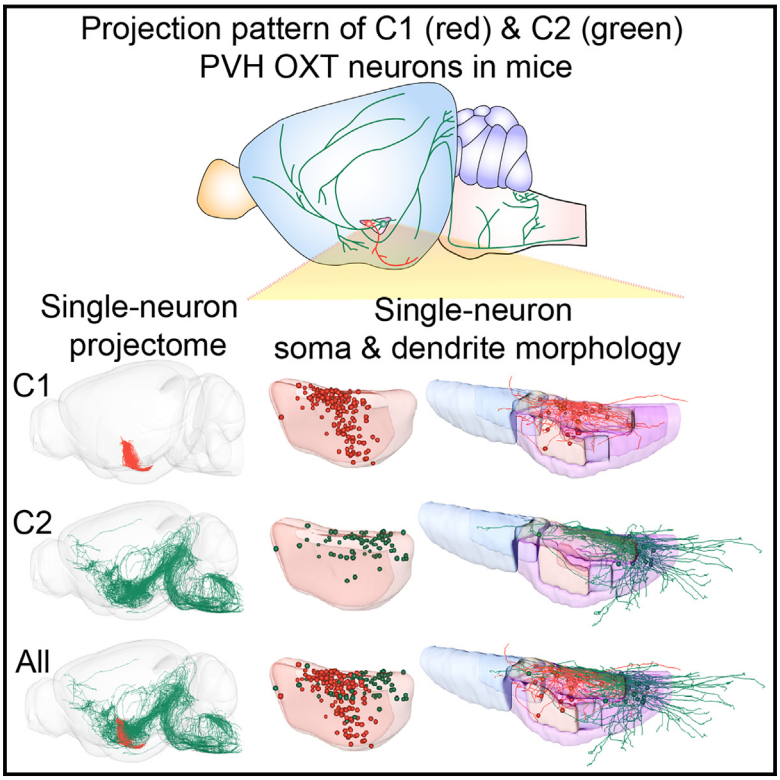

Authors

Humingzhu Li, Tao Jiang, Sile An, ..., Wen-Jie Bian, Anan Li, Xiang Yu

Correspondence

bianwenjie@westlake.edu.cn (W.-J.B.), aali@hust.edu.cn (A.L.), yuxiang01@pku.edu.cn (X.Y.)

In brief

Li et al. 3D reconstructed the complete axon, dendrite, and soma morphologies of individual OXT neurons in the mouse paraventricular hypothalamic nucleus at submicron resolution. They identified two main clusters, which project to mutually exclusive targets and possess distinct morphological features. These results provide a structural foundation for understanding OXT function.

Highlights

- 3D reconstruction of axon, dendrite, and soma morphologies of single OXT neurons
- ME-projecting C1 neurons do not have extrahypothalamic projections
- Non-ME-projecting C2 neurons co-project extensively to the endbrain and brainstem
- C1 and C2 neurons have distinct morphological and transcriptional characteristics

Li et al., 2024, Neuron *112*, 1081–1099
April 3, 2024
https://doi.org/10.1016/j.neuron.2023.12.022

CellPress

Neuron

CellPress

NeuroResource

Single-neuron projectomes of mouse paraventricular hypothalamic nucleus oxytocin neurons reveal mutually exclusive projection patterns

Humingzhu Li,[1,2,3,4,11] Tao Jiang,[5,11] Sile An,[6] Mingrui Xu,[2,7] Lingfeng Gou,[1] Biyu Ren,[1] Xiaoxue Shi,[1] Xiaofei Wang,[1] Jun Yan,[1,2] Jing Yuan,[5,6] Xiaohong Xu,[1,2] Qing-Feng Wu,[2,7] Qingming Luo,[5,6] Hui Gong,[5,6] Wen-Jie Bian,[1,8,9,*] Anan Li,[5,6,*] and Xiang Yu[1,2,3,4,10,12,*]

[1]Institute of Neuroscience and State Key Laboratory of Neuroscience, CAS Center for Excellence in Brain Science and Intelligence Technology, Chinese Academy of Sciences, Shanghai 200031, China
[2]University of Chinese Academy of Sciences, Beijing 100049, China
[3]School of Life Science and Technology, ShanghaiTech University, Shanghai 201210, China
[4]School of Life Sciences, Peking-Tsinghua Center for Life Sciences, and Peking University McGovern Institute, Peking University, Beijing 100871, China
[5]HUST-Suzhou Institute for Brainsmatics, JITRI, Suzhou 215123, China
[6]Britton Chance Center for Biomedical Photonics, Wuhan National Laboratory for Optoelectronics, MoE Key Laboratory for Biomedical Photonics, Huazhong University of Science and Technology, Wuhan 430074, China
[7]State Key Laboratory of Molecular Developmental Biology, Institute of Genetics and Developmental Biology, Chinese Academy of Sciences, Beijing 100101, China
[8]Westlake Laboratory of Life Sciences and Biomedicine, Hangzhou 310024, China
[9]School of Life Sciences, Westlake University, Hangzhou 310024, China
[10]Chinese Institute for Brain Research, Beijing 102206, China
[11]These authors contributed equally
[12]Lead contact
*Correspondence: bianwenjie@westlake.edu.cn (W.-J.B.), aali@hust.edu.cn (A.L.), yuxiang01@pku.edu.cn (X.Y.)
https://doi.org/10.1016/j.neuron.2023.12.022

SUMMARY

Oxytocin (OXT) plays important roles in autonomic control and behavioral modulation. However, it is unknown how the projection patterns of OXT neurons align with underlying physiological functions. Here, we present the reconstructed single-neuron, whole-brain projectomes of 264 OXT neurons of the mouse paraventricular hypothalamic nucleus (PVH) at submicron resolution. These neurons hierarchically clustered into two groups, with distinct morphological and transcriptional characteristics and mutually exclusive projection patterns. Cluster 1 (177 neurons) axons terminated exclusively in the median eminence (ME) and have few collaterals terminating within hypothalamic regions. By contrast, cluster 2 (87 neurons) sent wide-spread axons to multiple brain regions, but excluding ME. Dendritic arbors of OXT neurons also extended outside of the PVH, suggesting capability to sense signals and modulate target regions. These single-neuron resolution observations reveal distinct OXT subpopulations, provide comprehensive analysis of their morphology, and lay the structural foundation for better understanding the functional heterogeneity of OXT neurons.

INTRODUCTION

Studies of oxytocin (OXT) began with Sir Henry Dale administering extracts from the posterior pituitary (PPi) of oxen intravenously to mammals and observing facilitated uterine contractions.[1,2] In 1949, Bargmann provided convincing evidence that the axons that transport the extracts to the PPi came from hypothalamic regions, specifically the paraventricular hypothalamic nucleus (PVH) and supraoptic nucleus (SO),[3] thus turning the spotlight on the central nuclei secreting OXT. In 1954, du Vigneaud successfully synthesized the OXT nonapeptide, kick-starting the era for exploring OXT function. OXT is released both centrally and peripherally. Central release includes somatodendritic release into the ventricular circulation,[4–6] and axonal projections to central nuclei,[7–9] whereas peripheral release is through projections to the median eminence (ME)[10–12] and PPi[8,13,14]; all PPi projections passing through ME.

Functionally, OXT plays highly diverse roles, contributing to regulation of socio-emotional and socio-sexual behaviors, sensory processing, learning and memory, modulation of stress and pain systems, as well as homeostatic, metabolic, and autonomic responses.[15] Yet the structural basis of this functional

heterogeneity remains largely unknown. The somata of OXT neurons reside in the PVH, SO, and a number of accessory nuclei (AN),[8,16] both in and out of the hypothalamus.[17] PVH OXT neurons are the largest in number and also have the most extensive projections, encompassing all known OXT targets, including the endbrain (containing cerebral cortex and cerebral nuclei), thalamus, and hypothalamus, which together form the forebrain, as well as the brainstem and spinal cord.[17–20]

Several studies analyzed the mesoscale projection pattern of OXT neurons, especially PVH OXT neurons, using bulk labeling. Knobloch and colleagues[19] first demonstrated complex projection patterns of PVH OXT neurons in the rat endbrain and proposed that OXT neurons projecting to PPi have collaterals that project to forebrain regions. A subsequent study, also in rats, retrogradely labeled neurons innervating the PPi and found that they have collaterals projecting to multiple extrahypothalamic regions.[21] Another recent study, imaging and analyzing the mesoscale projectome of PVH OXT neurons through the entire mouse brain, found abundant projections in midbrain and hindbrain regions but relative sparse projections to the endbrain regions.[17]

Although illustrating the complexity of OXT neuron projection patterns, bulk labeling does not describe the diversity of individual OXT neuron projectomes, nor do they address whether subtypes of OXT neurons have distinct projection patterns or specific co-projection relationships, possibly aligned with function. Due to thresholding issues, brain regions with few projections may be missed in automated brain-wide quantification of bulk labeled samples. Most importantly, morphological characteristics of individual neurons cannot be extracted from mesoscale data, yet they are key to understanding the structural basis underlying functional heterogeneity of the OXT neuronal population.

To address the above questions, we imaged the whole-brain projectome of single OXT neurons at submicron resolution and 3D reconstructed the complete axonal morphologies of 264 sparsely and brightly labeled PVH OXT neurons. Two main clusters, which possess mutually exclusive projection patterns, as well as distinct morphological and transcriptional features, were identified by hierarchical clustering of projectomes. Morphological analysis of dendrites and somata revealed further differences between these clusters and among their subtypes. These observations significantly extend our knowledge of OXT neuronal morphology and provide a structural basis for understanding the complexity of OXT function.

RESULTS

Labeling and imaging PVH OXT neurons at submicron resolution

To visualize the whole-brain projectome of PVH OXT neurons, bright, sparse, and cell-type-specific labeling is essential. To this end, we generated rAAV-EF1α-DIO-YPet-p2A-mGFP, a Cre-dependent recombinant adeno-associated virus (rAAV), which expressed yellow fluorescent protein for energy transfer (YPet)[22] in tandem with a membrane-associated green fluorescent protein (mGFP). Infection of the PVH region of *Oxt-ires-Cre* mice with rAAV-EF1α-DIO-YPet-P2A-mGFP (Figure 1A) resulted in ~90% co-localization between fluorescent proteins and OXT immuno-reactivity (Figure 1B), suggesting high specificity of the rAAV in labeling OXT neurons (see STAR Methods for details). In samples used for single-neuron projectome analysis, 10%–20% of OXT neurons were labeled (Figure 1C).

Whole-brain image datasets were acquired using fluorescence micro-optical sectioning tomography (fMOST) technology[23,24] and included data from two channels: the GFP channel (channel 1 [CH1]) contained morphological information of OXT neurons; the propidium iodide (PI) channel (channel 2 [CH2]) contained cytoarchitectonic information. Images were registered to the 3D Allen mouse brain Common Coordinate Framework, version 3 (CCFv3) (see STAR Methods for details) to obtain accurate transformation parameters, and coronal sections (Figure S1) were checked for registration accuracy. The Fast Neurite Tracer (FNT) software[25] was used to compress images and reconstruct the dendritic and axonal morphologies of OXT neurons (Videos S1 and S2). 264 manually reconstructed axons passed quality control (see STAR Methods for details), including 115, 65, and 84 neurons from samples 18696, 195037, and 195038, respectively, and were registered to CCFv3 using the source brain's transformation parameters. Projection strength (please see below) of each axon in each brain region was quantitated and used for projectome classification. Soma reconstruction and PVH subdivision extraction were carried out using Amira, referencing the Allen Reference Atlas (ARAv2). Soma position and local dendrite connectivity were further analyzed according to projectome classification (Figure 1D).

Two clusters of PVH OXT neurons project to mutually exclusive targets

The axonal fibers of 264 traced neurons mapped to 214 brain regions (some CCFv3 regions were combined; please see Table S1 for list), including 172 regions with terminals (target regions), and additional regions with passing through fibers only. We separately quantified projection strength (total length of single fiber in each region) and total number of terminals in each analyzed region; the two parameters were highly correlated (R^2 = 0.904, $p < 0.0001$). Unsupervised hierarchical clustering of single-neuron projectomes (Figures 2A–2C; Tables S2 and S3; Video S3) generated two clusters, as recommended by R NbClust (see STAR Methods for details).[26] Cluster 1 (C1) contained reconstructed axons of 177 neurons terminating in ME; cluster 2 (C2) comprised axons of 87 neurons with more extensive arborizations, terminating in the forebrain, midbrain, pons, cerebellum, and medulla, but without terminals in ME. Measuring similarity between single-neuron projectomes using Canberra distance (Figure 2D), C1 neurons were more homogeneous than C2 neurons. Examples of C1 and C2 registered axons in CCFv3 outline are shown in Figure S2.

Next, we systematically analyzed correlation between the 214 regions based on projection strength and performed subsequent hierarchical clustering (Figure S3A; Table S4). Two regions mainly innervated by C1 neurons, ME and arcuate hypothalamic nucleus (ARH) (adjacent in Figure S3A, marked by blue arrow), had strong negative correlations with regions innervated by C2 neurons (midbrain reticular nucleus [MRN] and periaqueductal gray [PAG], respectively, top and bottom green boxes). In the correlation matrix of projection targets (Figure S3B; Table S5), ME (blue arrow) also exhibited strong negative correlation with MRN ($p < 0.01$) and PAG ($p < 0.01$) (green box in Figure S3B

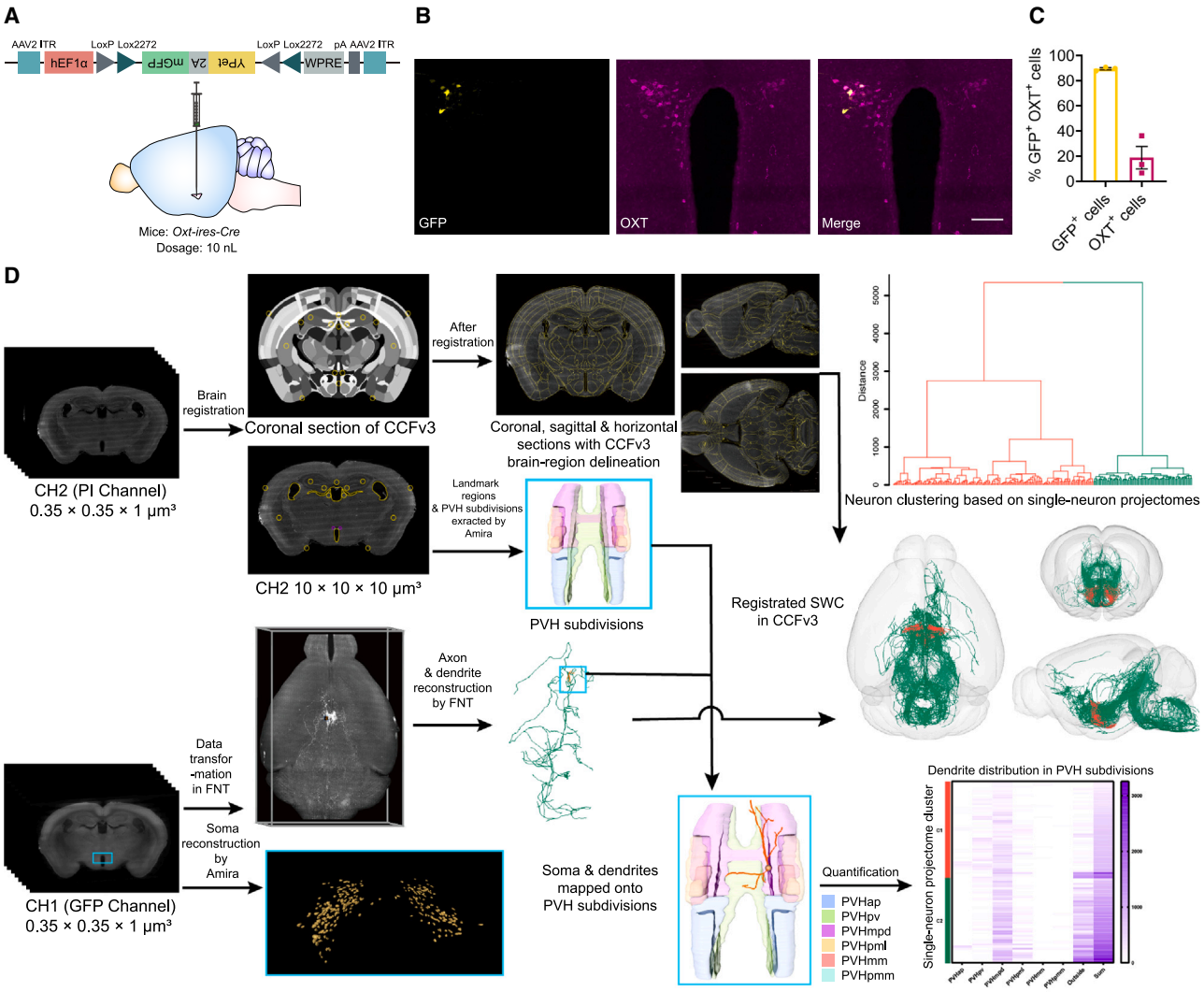

Figure 1. Pipeline for sparse labeling, whole-brain imaging, reconstruction, registration, and analysis of PVH OXT neurons

(A) Schematic showing the labeling strategy, injecting *Oxt-ires-Cre* mice with a low dose of bright and photostable rAAV-EF1α-DIO-YPet-p2A-mGFP in the PVH.

(B) Representative confocal images showing co-localization between sparsely labeled Ypet-p2A-mGFP-expressing neurons (GFP) and OXT immunostaining in the PVH. Scale bars, 100 μm.

(C) Quantitation of the proportion of GFP-expressing OXT neurons (GFP^+ OXT^+) with respect to total GFP-expressing neurons (GFP^+) or OXT-expressing neuron (OXT^+) of the PVH (n = 3 mice).

(D) Workflow of whole-brain fMOST dataset processing and analysis. Each fMOST dataset included two channels: the GFP channel (CH1) and the propidium iodide (PI) channel (CH2). Yellow circles superimposed on CCFv3 coronal section, and CH2 image represent features selected for registration. Subdivisions of PVH were extracted from CH2 images. CH1 images were used for reconstruction of single-neuron dendrites and axonal fibers using FNT and for soma reconstruction using Amira. OXT neurons were clustered based on single-neuron projectomes. Reconstructed dendrites and somata were mapped onto PVH subdivisions to analyze their distribution.

See also Figure S1 and Videos S1 and S2.

contains both regions), which are targeted extensively by C2 neurons. Similar negative correlations were observed in projection strength analysis (green boxes in Figure S3A). This mutually exclusive targeting of ME (C1) and non-ME (C2) projecting PVH OXT neurons confirmed our unsupervised hierarchical clustering results (Figures 2A–2D). Please see the discussion section for differences between our results and previous studies.

Having divided PVH OXT neurons into 2 clusters, we next characterized differences in their soma, dendrite, and axon morphology. As C1 neurons projected exclusively within the hypothalamus, their axons were significantly shorter and less complex than those of C2 neurons and targeted fewer brain regions (Figures 2E–2G). In addition, C2 neurons also had more primary dendrites, as compared with C1 neurons (Figure 2L). Registered soma center coordinates showed that C2 neurons distributed more posteriorly and more dorsally, as compared with C1 neurons (Figures 2H, 2J, and 2K). No major differences were observed between the two clusters in terms of volume, surface

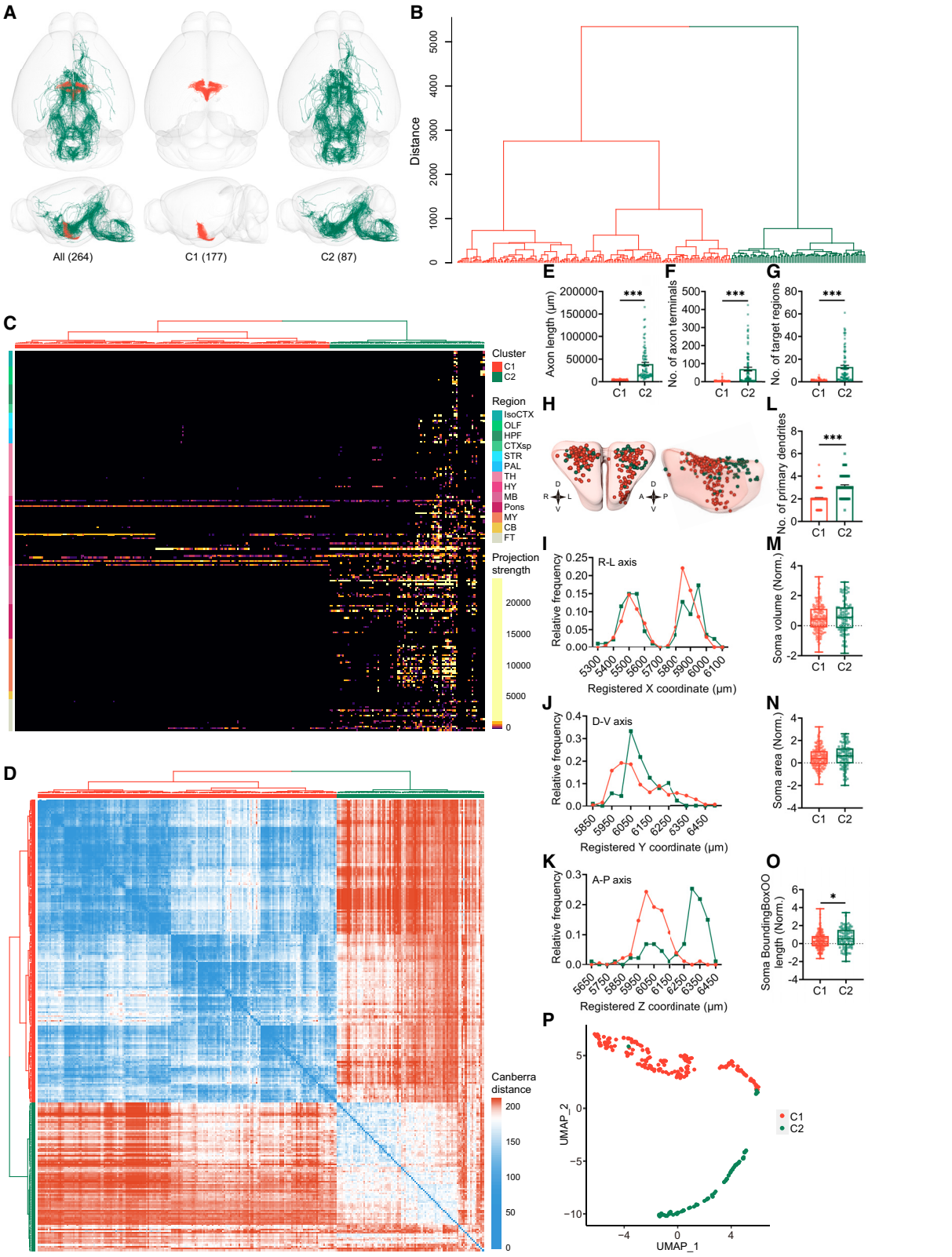

(legend on next page)

area, and right-left distribution of the reconstructed soma (Figures 2I, 2M, and 2N), except that C2 somata were slightly longer than C1 somata (Figure 2O).

Analyzing morphological measurements using uniform manifold approximation and projection (UMAP) also yielded two clusters (see STAR Methods for details), segregated essentially according to their projectome patterns (Figure 2P), independently confirming the results of unsupervised hierarchical clustering. Together, these results showed that PVH OXT neurons can be divided into two clusters, which project to mutually exclusive targets, possess distinct morphological features, and have spatially segregated somata.

Using molecular markers to further characterize C1 and C2 neurons

The next immediate question is whether the C1 and C2 morphological classifications align with known transcriptional signatures of PVH OXT neurons. A previous study using fluorescence-activated cell sorting (FACS)-sorted OXT neurons identified 181 genes significantly differentially expressed between magnocellular and parvocellular OXT neurons.[27] Magnocellular and parvocellular are classical classifications of OXT neurons, based on projection patterns, soma position, and electrophysiological properties.[16,28] To a first approximation, C1 and C2 neurons are, respectively, more similar to magnocellular and parvocellular cells (please see the discussion section for more details).

To determine if the transcriptional signatures of C1 and C2 neurons align with those of magnocellular and parvocellular OXT neurons, we injected FluoroGold (FG) intraperitoneally and injected cholera toxin subunit B (CTB) into the nucleus of the solitary tract (NTS, one of many targets of C2 neurons) to label the two cell types respectively. *In situ* hybridization of 9 signature genes, including 4 for magnocellular neurons, namely, calbindin 1 (*Calb1*), proprotein convertase subtilisin/kexin type 1 (*Pcsk1*), nitric oxide synthase 1, neuronal (*Nos1*), and tyrosine hydroxylase (*Th*), and 5 markers of parvocellular OXT neurons, namely reelin (*Reln*), netrin G1 (*Ntng1*), prodynorphin (*Pdyn*), secretogranin II (*Scg2*), and preproenkephalin (*Penk*), was performed, together with *Oxt*[29] (Figures 3A–3D and S4A–S4G). Quantitation across the PVH showed that neurons co-expressing *Calb1* and *Oxt* were mostly FG^+ (87%) (Figure 3C), whereas neurons co-expressing *Oxt* and *Reln* were mostly FG^- (95%) (Figure 3D). CTB did not colocalize with FG; neurons co-expressing *Calb1* and *Oxt* neurons were not labeled with CTB, whereas 11% of neurons co-expressing *Reln* and *Oxt* were labeled with CTB (Figures 3C and 3D). Of the other makers examined, *Pcsk1* and *Nos1* were relatively specific for C1 and magnocellular OXT neurons, whereas *Th* was less so (Figures S4A–S4C). For C2 and parvocellular OXT neuron markers, *Ntng1* colocalized with CTB and *Oxt* but not FG, whereas *Pdyn*, *Scg2*, and *Penk* were less specific (Figures S4D–S4G). Together, the above results show that magnocellular OXT marker *Calb1* and parvocellular OXT marker *Reln* also serve as markers of C1 and C2 neurons, respectively.

Morphological characters of C1 neuronal subtypes

Having shown that C1 and C2 neurons have distinct transcriptional signatures, we further characterized their morphology. We used unsupervised hierarchical clustering based on single-neuron projectomes to divide C1 neurons into subtypes C1-1, C1-2, and C1-3 (Figures 4A and 4F), respectively, containing 79, 53 and 45 neurons (Figures S2A–S2C). Neurons of C1-1 subtype have the shortest axons (Figure 4B); C1-3 neurons have more primary dendrites than C1-2 (Figure 4E); C1-2 neurons have more complex axons and target more diverse regions than C1-1 and C1-3 (Figures 4C and 4D). Although most C1-1 (86%) and C1-3 (89%) neurons terminated exclusively within ME, less than half of C2-2 (49%) neurons do so. Small differences were also observed in soma length and spatial distribution among subtypes (Figures 4G–4M). UMAP analysis did not separate subtypes according to projection patterns (Figure 4N).

A major advantage of single-neuron projectomes is the capacity to analyze co-projection patterns between target regions, reflected as high correlations between regions. We focused subtype analyses on projection target correlation matrices, as there is strong evidence for OXT release in target regions.[19,30] In C1-1 neurons, ARH and retrochiasmatic area (RCH) positively correlated with tuberal nucleus (TU) (Figure 4O); in C1-2 neurons (Figure 4P), ARH, lateral hypothalamic area (LHA) and TU highly correlated with each other, whereas PVH highly correlated with RCH and perifornical nucleus (PeF); in C1-3 neurons, ARH, TU,

Figure 2. Two clusters of PVH OXT neurons have mutually exclusive projection patterns and distinct morphologies

(A) Horizontal and sagittal views of the projectomes of PVH OXT neurons from cluster 1 (C1) and cluster 2 (C2); numbers of neurons in parentheses. The same cluster colors are used for all panels in this figure.

(B) Hierarchical clustering of PVH OXT neurons based on single-neuron projectomes. The y axis is distance between clusters. Numerical identifications of all neuron are listed in order in Table S2.

(C) Projectome matrix sorting neurons by cluster assignment. Each column represents one neuron; rows represent brain regions color-coded by brain divisions, order as in Table S3. Heatmap colors (quantile breaks) represent projection strengths (μm, single-neuron axon length in each brain region).

(D) Dissimilarity matrix of single-neuron projectomes. Columns and rows represent individual neurons sorted by cluster assignment. Heatmap colors represent Canberra distance between pairs of single-neuron projectomes.

(E–G) Comparison of axon lengths (E), number of axon terminals (F), and number of target regions (G) between C1 and C2 neurons; Mann-Whitney test.

(H) Soma distributions of C1 and C2 neurons in CCFv3 PVH (coronal and sagittal views).

(I–K) Somata position along right–left (I, $p = 0.292$), dorsal–ventral (J, $p < 0.001$), and anterior–posterior (K, $p < 0.001$) axes; Kolmogorov-Smirnov test.

(L) Comparison of numbers of primary dendrites between C1 and C2 neurons; Mann-Whitney test.

(M–O) Comparison of soma volumes, soma areas, and soma BoundingBoxOO lengths between C1 and C2 neurons; Student's unpaired t test. In this and subsequent boxplots, box edges represent 25th and 75th percentiles, the middle line represents the median, and whiskers mark the smallest and largest values.

(P) UMAP representation of traced morphological characteristics, including axon lengths, number of axon terminals, number of target regions, number of primary dendrites, soma volumes, soma areas, soma BoundingBoxOO lengths, and soma registered Y and Z coordinates.

Data are presented as mean ± SEM; *$p < 0.05$, **$p < 0.01$, ***$p < 0.001$.

See also Figures S2 and S3, Tables S1, S2, S3, S4,and S5, and Video S3.

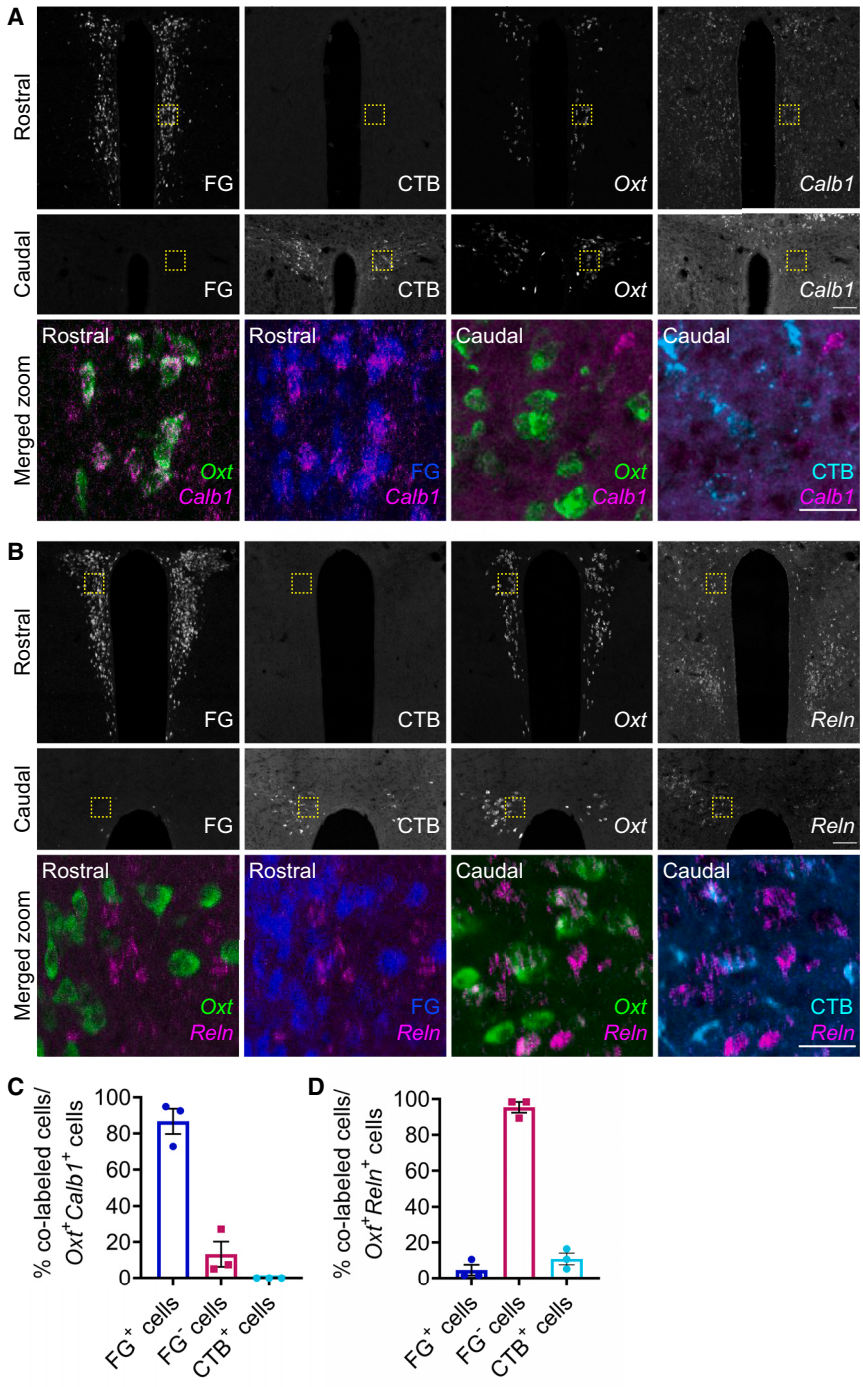

Figure 3. Molecular markers of C1 and C2 neurons

(A and B) Representative confocal images of PVH rostral (first row) and caudal (second row) sections for validating *Calb1* (A) and *Reln* (B) expression in mice injected with CTB into NTS and FG intraperitoneally (scale bars, 100 μm). Third row shows high-magnification merged images, positions as marked by yellow box. Marker genes, magenta; *Oxt* neurons, green; FG-labeled neurons, blue; CTB-labeled neurons, cyan. Scale bars, 30 μm.

(C and D) Quantitation of *Calb1* (C) and *Reln* (D) expression in PVH.

Data are presented as mean ± SEM.

See also Figure S4.

PeF, anterior hypothalamic nucleus (AHN) and PVH, descending division (PVHd) all highly correlated with each other (Figure 4Q). In other words, the three C1 subtypes show distinct projection trajectories to overlapping target sets.

In summary, our analysis showed that OXT neurons projecting to ME extended axonal arbors to other hypothalamic regions, including AHN, PVHd, PVH, RCH, ARH, LHA, and TU, in order of increasing terminal numbers. These projection patterns suggest potential regulation of central functions, such as circadian rhythm[31] and energy metabolism,[32] by ME-projecting neurons, in addition to their known peripheral neuroendocrinal functions.

Morphological characters of C2 neuronal subtypes

Unsupervised clustering based on single-neuron projectomes classified C2 neurons into three subtypes (Figures 5A, 5B, and S2D–S2F; Video S4). The C2-1 subtype (38 neurons) had the simplest projectome of this cluster, as indicated by fewest axon terminals and target regions, whereas the C2-2 axons (34 neurons) were the longest and innervated the most target regions (Figures 5C–5E). 15 neurons comprised the C2-3 subtype with heterogeneous projectome complexity, fewer primary dendrites than C2-1, and the smallest somata (Figures 5C–5I). There were no significant differences in right-left or dorsal-ventral distribution of C2 somata (Figures 5J–5L); more C2-1 neurons localized to posterior PVH (Figure 5M). UMAP analysis showed two main clusters: one mostly containing C2-1 neurons and another mostly containing C2-2 neurons; C2-3 neurons were interspersed between the two clusters (Figure 5N).

C2-1 neuron target regions and co-projection matrix

The C2-1 projection target correlation matrix contained 38 regions, grouped into 10 units based on hierarchical clustering using the Ward aggregation method (Figure S3C; Table S6 for complete list and unit grouping). Some units contained highly correlated brain regions, which likely are co-projected by the same neuron. For this and subsequent subtypes, we describe the two most prominent units, chosen based on high correlation strengths and existing knowledge of target function. For C2-1 neurons, the first unit (5 brain regions, green box in Figures 5O and S3C) included the nucleus raphe pallidus (RPA), nucleus raphe obscurus (RO), magnocellular reticular nucleus (MARN),

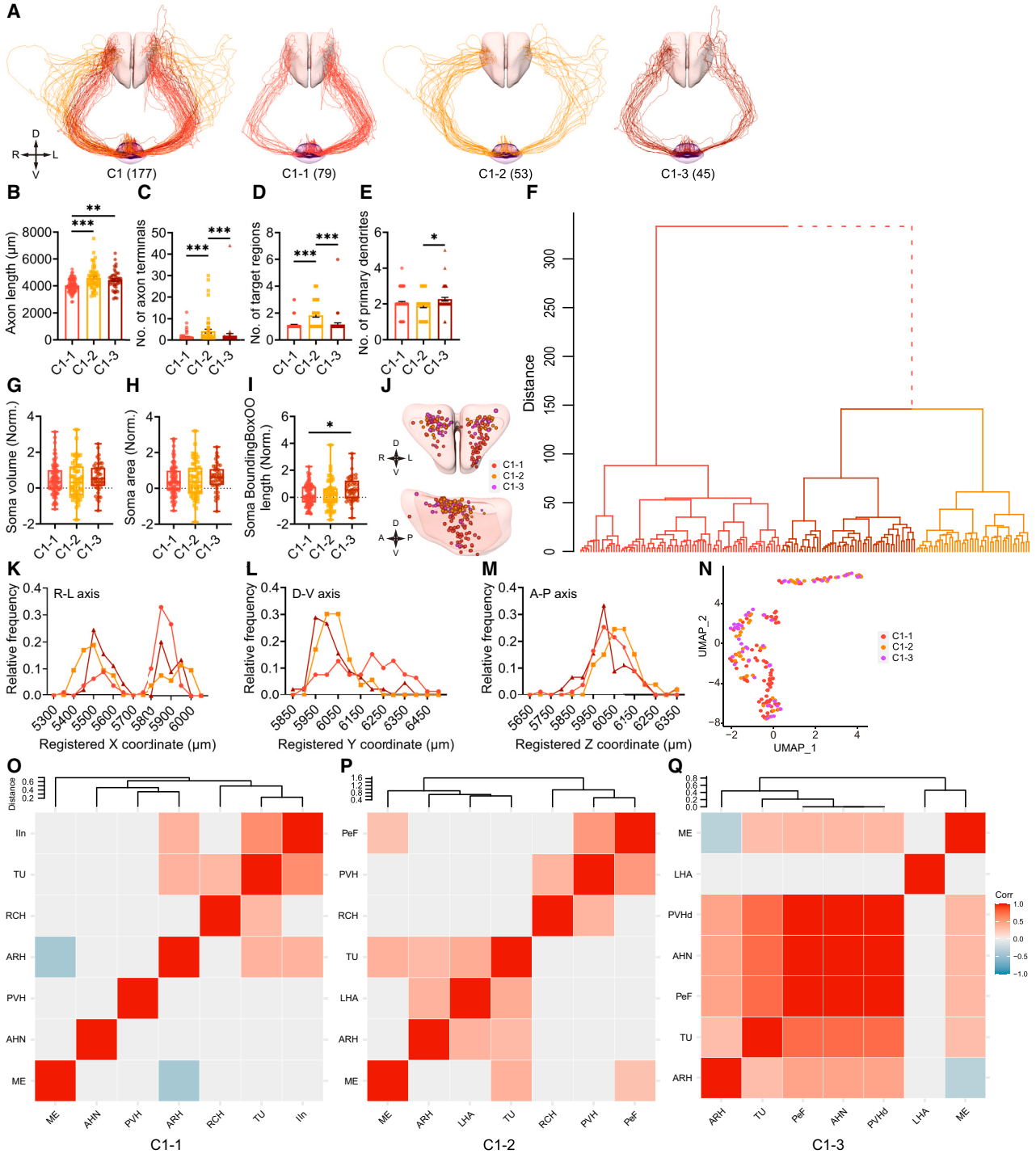

Figure 4. Morphological characterization of C1 neuronal subtypes

(A) Coronal views of individual C1 axons in each subtype (numbers of neurons in parentheses). Pale pink (top) and purple (bottom) structures represent the PVH and ME, respectively. (A)-(I) and (K)–(M) use the same subtype colors.

(B–E) Comparison of axon lengths (B), number of axon terminals (C), number of target regions (D), and number of primary dendrites (E) among C1 subtypes; one-way ANOVA with Tukey's post hoc test (B) or Kruskal-Wallis test with Dunn's post hoc test (C–E).

(F) Hierarchical clustering of C1 neurons based on single-neuron projectomes. The y axis is distance between clusters.

(G–I) Comparison of soma volumes (G), soma areas (H), and soma BoundingBoxOO lengths (I) among C1 subtypes; one-way ANOVA with Tukey's post hoc test.

(J) Soma distribution of C1 neuronal subtypes in CCFv3 PVH (coronal and sagittal views).

(legend continued on next page)

and nucleus raphe magnus (RM), all components of the reticular formation, which play important roles in receiving sensory inputs, movement, and autonomic control[33]; it also included the dorsal roots (drt), which carries suckling information from the spinal cord to the hypothalamus.[34]

The second unit (9 regions, blue box in Figures 5O and S3C), included the parabrachial nucleus (PB) and PAG, as well as PVHd and ARH, which are involved in autonomic regulation[35–38]; inferior colliculus (IC) integrates information from ascending auditory pathways, descending corticotectal projections, intercollicular pathways, and extra-auditory sources, especially the somatosensory system[39]; corticospinal tract (cst) carries movement-related information from the brain to the spinal cord; dorsal nucleus raphe (DR) controls various physiological functions, including learning, memory and affect[40]; vestibulocochlear nerve (VIIIn) transfers motor information[41]; mammillary body (MBO) is involved in spatial and episodic memory consolidation, as well as fear response, reward and goal-directed behaviors.[42]

In summary, the terminals of C2-1 neurons mostly project to regions involved in motor and autonomic control, as well as sensory information processing and transfer.

C2-2 neuron target regions and co-projection matrix

The C2-2 projection target correlation matrix contained 163 regions, grouped into 15 units; they have the largest target region number of any subtype (Figure S3D; Table S7). Two prominent units with high correlation within and between units were further analyzed. The first unit contained 5 regions (green box in Figures 5P and S3D), including the prelimbic area (PL), orbital area (ORB), basomedial amygdalar nucleus (BMA), frontal pole cerebral cortex (FRP), and somatomotor areas (MO). The second unit comprised 17 regions (blue box in Figures 5P and S3D), including the pretectal region (PRT), posterior intralaminar thalamic nucleus (PIL), subparafascicular nucleus, magnocellular part (SPFm), olfactory tubercle (OT), caudoputamen (CP), posterior amygdalar nucleus (PA), claustrum (CLA), hippocampo-amygdalar transition area (HATA), prosubiculum (ProS), dentate gyrus (DG), hippocampal CA3 and CA1, nucleus of the lateral olfactory tract (NLOT), taenia tecta (TT), anterior olfactory nucleus (AON), infralimbic area (ILA), and agranular insular area (AI).

As compared with other subtypes, C2-2 neurons target more to the cerebral cortex and cerebral nuclei regions. Since the two units have overlapping functions and are highly correlated with each other, we summarize the combined reported function as follows: (1) learning and memory, by regions including CA1, CA3, DG, ProS, and HATA of the hippocampal formation; (2) odor-dependent social recognition, including AON, OT, NLOT, TT, PL, ILA, and ORB[43]; (3) nociceptive regulation, including AI,[44] MO,[45] and PRT[46]; (4) sensory processing and movement, including PA,[47] PIL,[48] and SPFm.[49]

C2-3 neuron target regions and co-projection matrix

The C2-3 projection target correlation matrix contained 76 regions, including 10 units (Figure S3E; Table S8), two of which we described in detail. The first unit (15 regions, green box in Figures 5Q and S3E) included reticular formation components, such as the paragigantocellular reticular nucleus (PGRN) and gigantocellular reticular nucleus (GRN), respectively, involved in eye and head movement,[50] and both conveying nociceptive messages[51]; intermediate reticular nucleus (IRN) relays respiratory information[52]; medial amygdalar nucleus (MEA) relays olfactory information to central amygdalar nucleus (CEA), whereas CEA integrates diverse sensory information to regulate autonomic and nociceptive behaviors[53]; central lobule (CENT) relays somatosensory information; pedunculopontine nucleus (PPN) and anterior amygdalar area (AAA) contain cholinergic neurons and may be involved in arousal function[54,55]; pontine central gray (PCG) is involved in aversive behaviors.[56]

The second unit (14 regions, blue box in Figures 5Q and S3E) included DR and laterodorsal tegmental nucleus (LDT), containing serotonergic and cholinergic neurons, respectively, which together with MRN, are involved in sensory information relay and cortical activation during arousal[57]; retrorubral area (RR) contains dopaminergic neurons[58]; superior colliculus, motor related (SCm) plays important roles in motor control.[59]

Some C2-3 neurons also target endbrain and brainstem regions, but less extensively than C2-2 neurons. The projection patterns of C2-3 neurons suggest that they have important functions in arousal, and sensory information relay and integration.

C2 subtypes have different target region preferences (Figures S5A and S5B; Table S9). For example, 79% of C2 neurons project to MRN, including 84% of C2-1, all of C2-2, and 20% of C2-3 neurons; 65% of C2-2 and 24% of C2-1 neurons project to the ventral tegmental area (VTA), whereas C2-3 neurons do not; and 59% of C2-2 neurons project to NTS, whereas C2-1 or C2-3 neurons do not. We also present the number of neurons with fibers or terminals in each target region (Figure S5C; Table S9).

The complexity of the projection matrix of C2 neurons, with each neuron projecting to brain regions with multiple known functions, is consistent with the physiological function of OXT in regulating complex behaviors.

Correlated single-neuron and mesoscale projectomes

Do the projection patterns of the 264 traced neurons recapitulate the mesoscale projectome of PVH OXT neurons? In other words, did we trace enough neurons to obtain a representative sample of the projectome of PVH OXT neurons? To examine this, we injected virgin female, lactating female, and male *Oxt-ires-Cre* mice with rAAV-EF1α-DIO-YPet-P2A-mGFP to bulk label PVH OXT neurons. The groups were chosen to assess whether sex or lactating experience affected the projection patterns of OXT

(K–M) Frequency distribution of registered X (K), Y (L), and Z (M) coordinates of C1 subtype somata. (K) C1-1 vs. C1-2, $p < 0.05$, Kruskal-Wallis test with Dunn's post hoc test; (L) C1-1 vs. C1-2 and C1-1 vs. C1-3, $p < 0.001$, Kruskal-Wallis test with Dunn's post hoc test; (M) C1-1 vs. C1-2, $p < 0.05$ and C1-2 vs. C1-3, $p < 0.01$, one-way ANOVA with Tukey's post hoc test.

(N) UMAP representation of C1 neuron subtypes.

(O–Q) Projection target correlation matrices showing the Spearman's rank correlation coefficient between pairs of target regions with C1-1 (O), C1-2 (P), and C1-3 (Q) neuron axonal terminals. Non-significant correlation coefficients are shown in gray to emphasize significant correlations ($p < 0.05$). The y axis is distance between clusters. Data are presented as mean ± SEM; *$p < 0.05$, **$p < 0.01$, ***$p < 0.001$.

See also Figure S2.

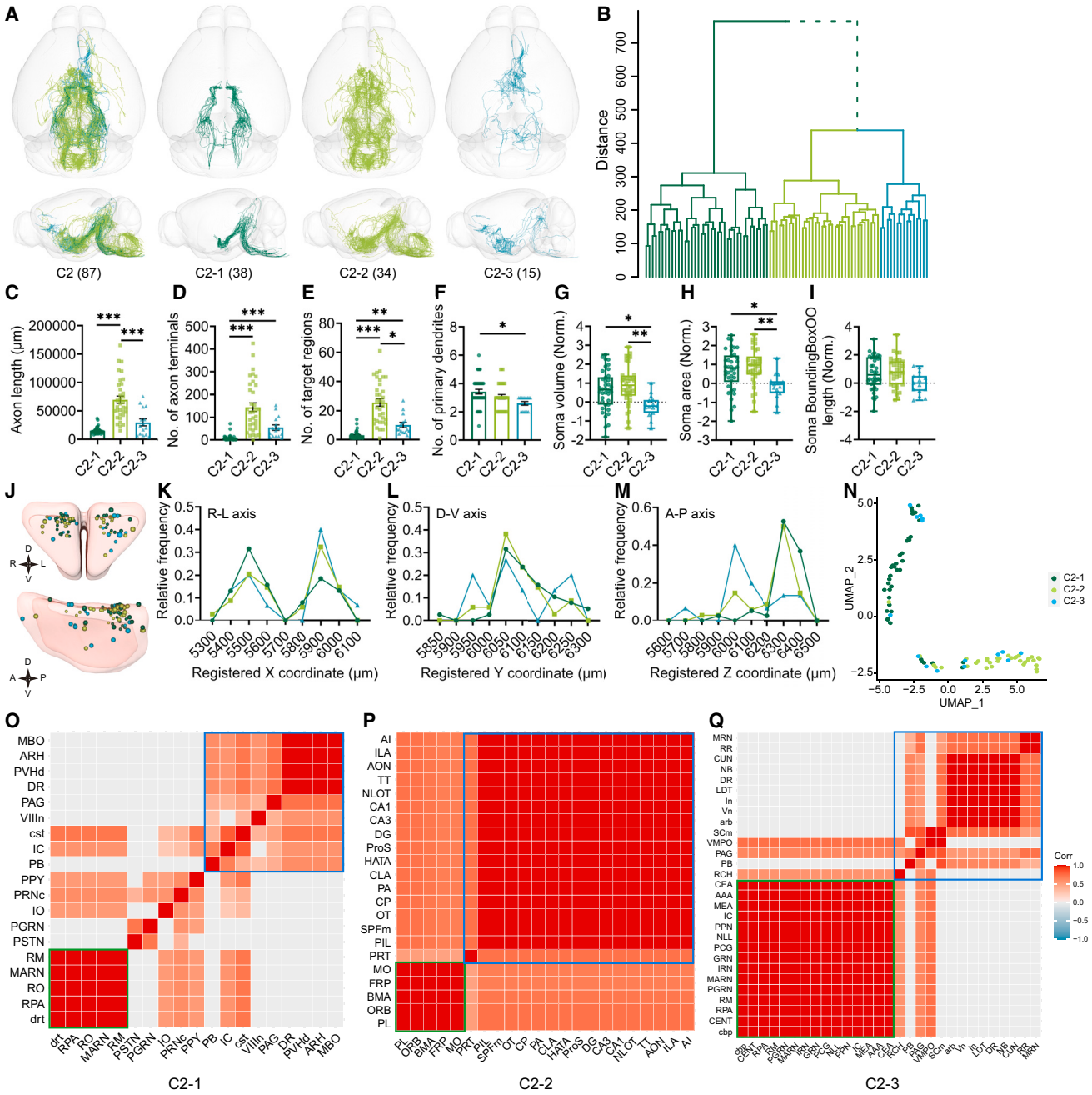

Figure 5. Morphological characterization of C2 neuronal subtypes

(A) Horizontal and sagittal views of C2 axons in each subtype (numbers of neurons in parentheses). (A)–(N) use the same C2 subtype colors.

(B) Hierarchical clustering of C2 neurons based on single-neuron projectomes. The y axis is distance between clusters.

(C–F) Comparison of axon lengths (C), number of axon terminals (D), number of target regions (E), and number of primary dendrites (F) among C2 subtypes; Kruskal-Wallis test with Dunn's post hoc test.

(G–I) Comparison of soma volumes (G), soma areas (H), and soma BoundingBoxOO lengths (I) among C2 subtypes; one-way ANOVA with Tukey's post hoc test.

(J) Soma distribution of C2 neuronal subtypes in PVH (coronal and sagittal views) in CCFv3.

(K–M) Frequency distribution of registered X (K), Y (L), and Z (M) coordinates of C2 subtype somata. (M) C2-1 vs. C2-2 $p < 0.05$ and C2-1 vs. C2-3 $p < 0.001$, Kruskal-Wallis test with Dunn's post hoc test.

(N) UMAP representation of C2 neuron subtypes.

(O–Q) A zoomed region of projection target correlation matrices, showing the Spearman's rank correlation coefficient between pairs of target regions with C2-1 (O), C2-2 (P), and C2-3 (Q) neuron axonal terminals; brain regions ordered as in Table S6, S7, and S8. Non-significant correlation coefficients are shown in gray. Green and blue boxes outline clustered brain regions.

Data are presented as mean ± SEM; *$p < 0.05$, **$p < 0.01$, ***$p < 0.001$.

See also Figures S2, S3, and S5, Tables S6, S7, S8, and S9, and Video S4.

neurons. 36 brain regions, selected based on previously reported functions of OXT, were manually delineated and quantitated from fMOST images (see STAR Methods for details). No significant differences in projection patterns were observed among the three groups, consistent with the result of a recent report[17] (Figure S6A).

To analyze correlation with single-cell projectome, we calculated the whole-brain mesoscale projection intensity (MPI) of bulk labeled sample 16454 in all regions with OXT fibers (263 regions in total, Table S10) and compared it with the single-neuron projection intensity (snPI) of the 264 reconstructed neurons in these regions. The coefficient of determination and Spearman's rank correlation coefficient were 0.603 ($p < 0.001$) and 0.840 ($p < 0.001$), respectively (Figures S6B and S6C). This significant correlation provided strong evidence that our single-neuron projectomes are representative of the entire PVH OXT population, suggesting that we traced enough neurons to cover main projection subtypes of PVH OXT neurons. In a previous work analyzing single-neuron projectomes in the prefrontal cortex, 17–42 neurons were calculated to be sufficient to represent each cluster, and tracing more neurons (197–322 neurons per cluster) did not add significant information.[25]

Functional components of OXT neuron projectomes

Comparing projection patterns among PVH OXT neurons

To visualize and compare projection pattern of subtypes of PVH OXT neurons, we plotted their fiber and terminal distributions according to brain divisions. 97% of C1 neuron axon fibers and almost all their terminals distributed within hypothalamic regions; the fiber tract (2.8% of total axon length and one terminal), striatum, pallidum, and thalamus contained few C1 axon fibers (Figures 6A and 6B).

Axon fibers and terminals of C2 neurons distributed much more widely in the brain. C2-1 neuron axon distribution included: thalamus (2% of total axon length and 3% of all terminals), hypothalamus (31% and 9%), midbrain (29% and 31%), pons (16% and 19%), medulla (6% and 27%), and fiber tract (15% and 11%). Fibers and terminals of C2-2 neurons distributed in more brain regions, including the isocortex (1% and 2%), olfactory area (1% and 2%), hippocampal formation (0.8% and 1.4%), cortical subplate (0.3% and 0.5%), striatum (3% and 5%), pallidum (3% and 5%), thalamus (2% and 1%), hypothalamus (25% and 26%), midbrain (23% and 18%), pons (7.5% and 5%), medulla (26% and 29%), cerebellum (0.4% and 0.5%), and fiber tracts (7% and 6%). Notably, the proportion of C2-2 terminals in the endbrain is nearly double that of axon fibers; proportions of fibers and terminals were similar in other divisions. Axon fibers and terminals of C2-3 neurons distributed in the isocortex (3.2% and 3%), olfactory area (4% and 3%), hippocampal formation (0.2% and 0), striatum (6% and 5%), palladium (9% and 9%), thalamus (2.5% and 1%), hypothalamus (42% and 51%), midbrain (17% and 17%), pons (5% and 3%), medulla (2% and 3%), cerebellum (1% and 1%), and fiber tracts (8% and 4%). The proportion of total axon length and terminals was similar among all brain divisions.

In terms of lateralization, 5% of C2-1 neurons (2/38) projected to the contralateral hemisphere with 4% and 22% projection strengths, respectively, whereas other C2-1 neurons projected ipsilaterally. 88% of C2-2 neurons (30/34) extended axons contralaterally, on average 14% of their total projections. C2-3 neurons have the most diverse patterns: 13% (2/15) had 90% contralateral projections, 7% (1/15) had 59%, and 40% (6/15) had 9%, whereas the other 33% had none.

The most abundantly innervated divisions of C2-1, C2-2, and C2-3 neuronal subtypes were pons, medulla, and hypothalamus, respectively, suggesting differences in primary regulatory targets among C2 subtypes. Only C2-2 and C2-3 subtypes projected to the endbrain. Although most C1 total axon fibers and terminals are intra-hypothalamic, they are restricted to 18 regions, as compared with 37 and 34 regions of C2-2 and C2-3 neurons, respectively.

Projection targets for producing 5-HT, ACh, DA, and NE

A striking feature of the mesoscale projectome is the high intensity of OXT neuron projections in brain regions producing neuromodulators, including serotonin (5-HT), acetylcholine (ACh), dopamine (DA), and norepinephrine (NE). Correspondingly, target regions of single-neuron projectomes included serotoninergic neuron-containing regions the rostral linear nucleus raphe (RL), central linear nucleus raphe (CLI), DR, superior central nucleus raphe (CS), RM (B3med), RO (B2), RPA (B1), part of PGRN (B3lat) and GRN (B3lat), supragenual nucleus (SG, B4), nucleus raphe pontis (RPO, B5), B9[60]; cholinergic neuron-containing regions the diagonal band nucleus (NDB), medial habenula (MH), PPN, LDT, pontine gray (PG), oculomotor nucleus (III), trochlear nucleus (IV), motor nucleus of trigeminal (V), facial motor nucleus (VII), nucleus ambiguus (AMB), dorsal motor nucleus of the vagus nerve (DMX), and hypoglossal nucleus (XII)[61]; dopaminergic neuron-containing regions the VTA, substantia nigra, compact part (SNc), RR (A8), and A11, A12, A13, and A14; norepinephrinergic neuron-containing regions the locus ceruleus (LC), subceruleus nucleus (SLC), as well as A1, A2, A5, and A7.

Extracting the OXT neuron projectome data from these 27 brain regions, we found that the C2-2 neurons, with the most complex and extensive axonal arborizations, projected most highly to these regions (Figures 6C and 6D). Importantly, correlation matrix of both projection strength and targets showed that regions producing different types of neuromodulators had significant co-projection relationships. For example, PPN, which produces ACh, positively correlated with 4 regions producing 5-HT, 3 other regions producing ACh, and one region producing DA or NE. Early work in parturient ewes suggested that OXT release in the OB may facilitate olfactory recognition by modulating NE and ACh.[62] More recently, a study convincingly showed that OXT released from PVH coordinated with OXT-dependent 5-HT release from DR to regulate medium spiny neurons in the nucleus accumbens (ACB) during social reward.[63] PVH OXT neurons have been shown to act on VTA and SNc DA neurons to promote pro-social behavior.[64,65] OXT has also been shown to mediate the effects of 5-HT in infant affiliation behavior in mice, rats, and monkeys.[66] Our projectome results, together with the results of the above-mentioned functional studies, are consistent with extensive crosstalk between OXT and other neuromodulators.

Projections to other OXT neuron-containing brain regions

In addition to PVH and SO, OXT neurons are also present in a number of AN, including MEA, bed nuclei of the stria terminalis

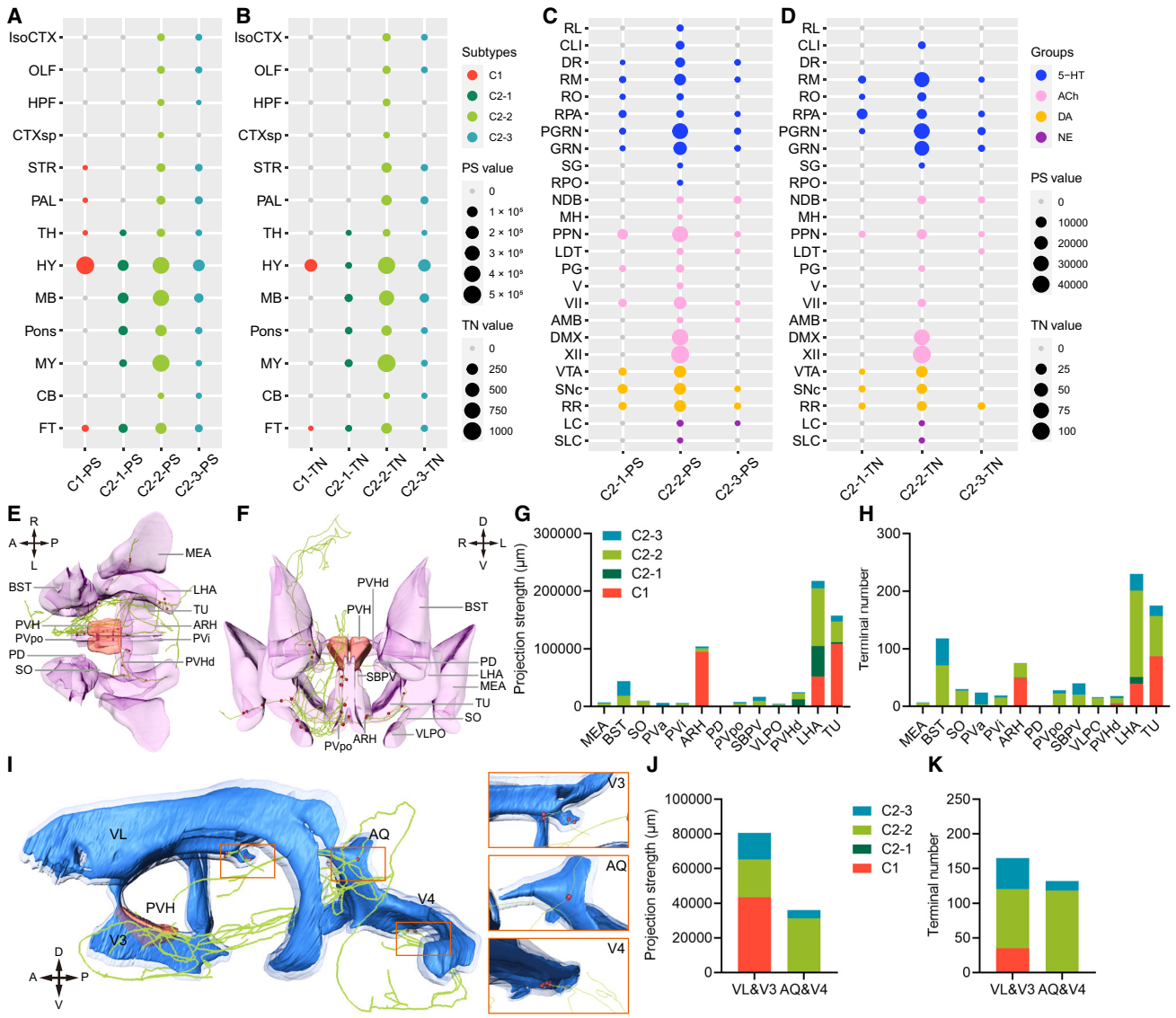

Figure 6. Functional components of OXT neuron projectomes

(A and B) Projection pattern of C1 (all together) and C2 subtypes according to total projection strengths (A) or terminal numbers (B) in each brain division. Dot size represents total projection strengths (A) or terminal numbers (B). Gray dots indicate lack of distribution.

(C and D) Projection strengths (C) and terminal numbers (D) of C2 neuronal subtypes in brain regions producing 5-HT, ACh, DA, and NE.

(E and F) Horizontal (E) and coronal (F) views of one C2-2 neuron projecting to other OXT neuron-containing brain regions. PVH and other regions containing OXT neurons are shown in 3D in pink and purple, respectively; abbreviations as in Table S1. Red dots represent axon terminals.

(G and H) Quantification of axon fiber and terminal distribution in other OXT-containing brain regions based on projection strengths (G) and terminal numbers (H).

(I) 3D view of one C2-2 neuron projecting near the ventricle system (blue). The light-blue outline represents a $50\sqrt{2}$ μm zone bordering the ventricle system. PVH is shown in pink; axon terminals in the border zone are shown as red dots. Zoomed views of axon terminals closed to V3, AQ, and V4 are shown on the right.

(J and K) Projection strengths (J) and terminal numbers (K) in the border zone.

(BST), periventricular hypothalamic nucleus, anterior part (PVa), periventricular hypothalamic nucleus, intermediate part (PVi), ARH, posterodorsal preoptic nucleus (PD), periventricular hypothalamic nucleus, preoptic part (PVpo), subparaventricular zone (SBPV), ventrolateral preoptic nucleus (VLPO), PVHd, LHA, and TU.[17] We thus quantified OXT projection strength and terminal numbers in these regions. Again, C2-2 neurons were the major source projecting to other OXT neuron-containing regions; ARH, LHA, and TU were densely targeted by C1 neurons as well (Figures 6E–6H).

Projections surrounding the ventricle system

When manually reconstructing axons, we noticed that some axons terminated in regions adjacent to the ventricle system. We thus delineated a $50\sqrt{2}$ μm[67] zone along the ventricle boundary to analyze the distribution of axon fibers and terminals in this zone. Neurons from all subtypes, except for C2-1, projected to

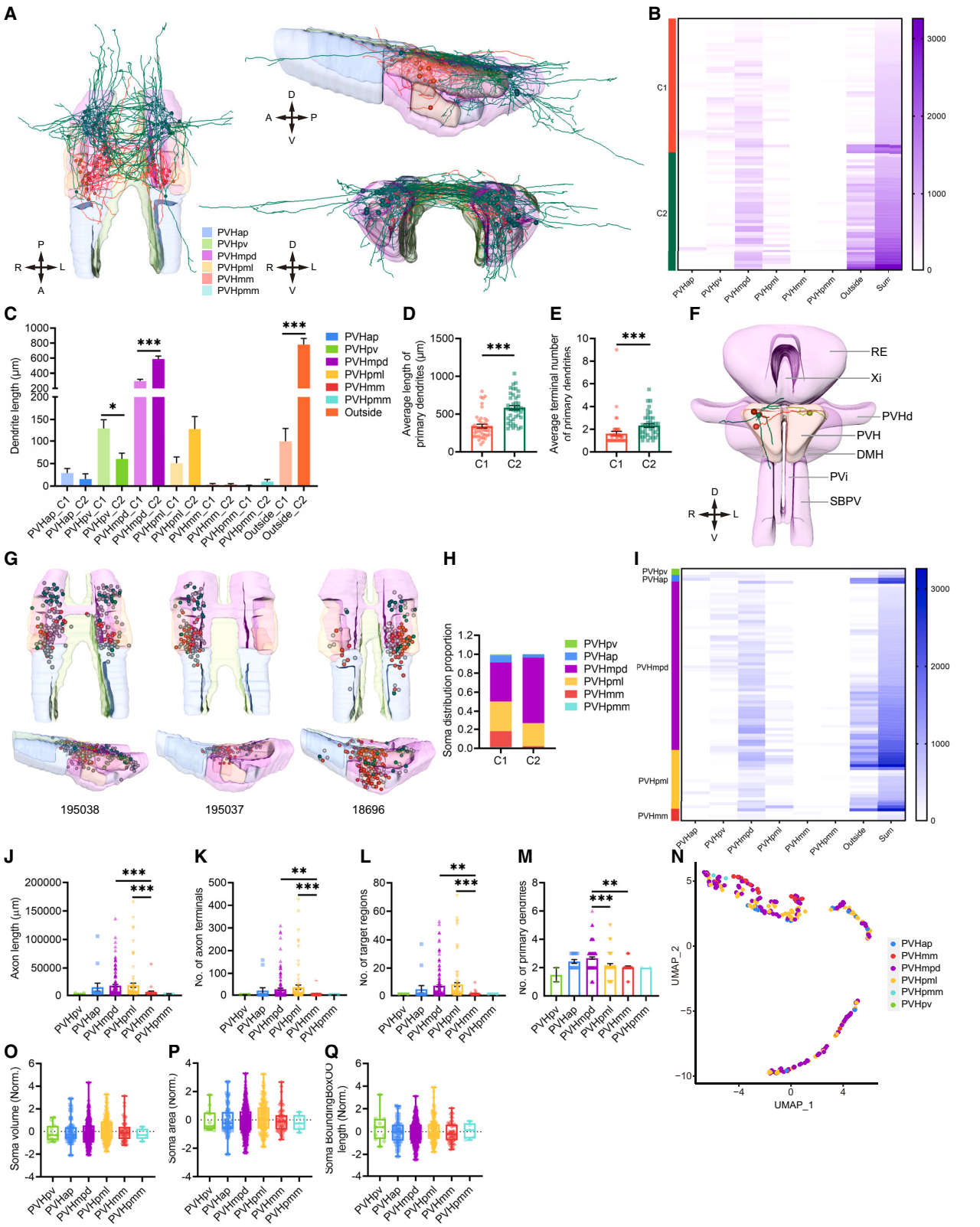

(legend on next page)

regions adjacent to the lateral ventricle (VL) and third ventricle (V3). C2-2 and C2-3 subtypes also projected to regions adjacent to the cerebral aqueduct (AQ) and the fourth ventricle (V4) (Figures 6I–6K). Although somatodendritic release of OXT into V3 is generally thought to be the main source of OXT in the cerebrospinal fluid (CSF), release from axons, especially those reaching VL, AQ, and V4, likely also contribute.

Dendritic morphology of C1 and C2 neurons

The somata of OXT neurons in one sparsely labeled sample (195038) were sufficiently dispersed to allow for dendrite reconstruction. The dendrites of all neurons with traced axons were reconstructed and mapped onto PVH subdivisions to analyze their distribution based on projectome clusters (Figure 7A). The dendrites of C1 neurons mostly distributed in the medial parvicellular part, dorsal zone (PVHmpd), and periventricular part (PVHpv) of the PVH parvicellular division, whereas those of C2 neurons mostly distributed in the PVHmpd or extended outside of PVH (Figure 7B). Comparing dendrite length of C1 and C2 neurons in subdivisions, significant differences were observed in PVHpv, PVHmpd, and in regions outside of PVH (Figure 7C). The dendrites of both C1 and C2 neurons project to extra-PVH regions, C1 dendrites extended to two thalamic regions, namely the nucleus of reuniens (RE) and xiphoid thalamic nucleus (Xi), as well as two hypothalamic regions, namely PVHd and AHN; C2 dendrites extended to these regions, as well as PVi, SBPV, dorsomedial nucleus of the hypothalamus (DMH), LHA, and zona incerta (ZI) (Figure 7F). In addition to having more primary dendrites than C1 neurons (Figure 2L), the primary dendrites of C2 neurons were longer and had more terminals (Figures 7D and 7E).

Morphological characterization of PVH subdivisions

Based on previous retrograding labeling experiments in rats and mice, distinct neuron morphological features, including soma size and projection targets, have been observed in different PVH subdivisions.[16,68] We thus mapped the labeled somata onto PVH subdivisions; most somata mapped to PVHmpd and PVH, magnocellular division, posterior magnocellular part, and lateral zone (PVHpml) (Figures 7G and 7H). Dendrites from neurons on both sides of the PVH had extensive projections to the middle of PVH, immediately above and closed to 3V, containing parts of PVHmpd and PVHpv. The anterior part of this area, close to C1 soma-residing region, contained dendrites from C1 and C2 neurons (Figures 7A and 7I), whereas the posterior part contained more exclusively dendrites of C2 neurons. The proximity of these dendrites to the ventricle makes release of OXT directly into the CSF possible.

As compared with somata in PVHmpd and PVHpml, somata in PVH, magnocellular division, and medial magnocellular part (PVHmm) had shorter axons, fewer axon terminals, and target regions (Figures 7J–7L). Somata in PVHmpd had more primary dendrites than PVHpml and PVHmm (Figure 7M). Other parameters were not significantly different among subdivisions (Figures 7O–7Q). In the UMAP analysis, somata in PVHmm were relatively concentrated in one cluster, whereas somata in other subdivisions were intermixed (Figure 7N).

DISCUSSION

Here, we reconstructed for the first time the single-neuron projectome of PVH OXT neurons at submicron resolution (Figure 8), clustered these neurons into 6 subtypes, and systematically analyzed the soma and dendrite characteristics of these subtypes, in the context of their PVH subdivision location. Based on our morphological characterization, some subtypes fitted neatly with previously described OXT functions: (1) C1 neurons have peripheral function of regulating neurohypophysis and adenohypophysis, as well as central functions regulating circadian rhythm and energy metabolism; (2) C2-1 neurons mostly have ipsilateral projections and mediate somatosensory, nociceptive, and analgesic regulations; and (3) C2-2 and C2-3 neurons, subtypes with the most complex arborizations and bilateral projection patterns, likely mediate most of the known "higher brain functions" of OXT, including sensation, social recognition, pro-social behavior, learning and memory, reward, and aggressive behavior following stress.

Correlations of C1 and C2 neurons with existing classifications of PVH OXT neurons

As previously mentioned, PVH OXT neurons are often classified as magnocellular and parvocellular neurons, based on projection patterns, soma position, and electrophysiological properties.[16,28]

Figure 7. Morphological characterization of C1 and C2 neuron dendrites and somata in PVH subdivisions

(A) Horizontal, sagittal, and coronal views of C1 and C2 neuron soma and dendrite distribution in PVH subdivisions. Somata and dendrites are cluster color-coded. The 3D PVH structure is color-coded as follows: PVHap, blue; PVHpv, green; PVHmpd, purple; PVHpml, yellow; PVHmm, red; PVHpmm, cyan.

(B and C) Comparison of C1 and C2 neuron dendrite distribution in PVH subdivisions. In the heatmap, rows represent neurons sorted by projectome clusters, columns represent subdivisions of PVH, and values denote the dendrite lengths (μm) per neuron in each subdivision (C, two-way ANOVA with Bonferroni post hoc test).

(D and E) Comparison of average lengths (D) and average terminal numbers of primary dendrites (E) between C1 and C2 neurons; Mann-Whitney test.

(F) Coronal views of the dendrite distribution of two C1 (red) and two C2 (green) neurons in PVH and extra-PVH regions. Somata and dendrites are subtype color-coded. The pale pink and purple 3D structures represent PVH and extra-PVH regions, respectively.

(G) Horizontal and sagittal views of soma locations in PVH subdivisions. 3D structures of PVH subdivisions are colored as in (A). Somata with reconstructed axons are cluster color-coded, those without projection information are shown in gray. The sample number is shown at the bottom.

(H) Soma distribution of C1 and C2 neurons in PVH subdivisions.

(I) Quantification of dendrite distribution in PVH subdivisions according to soma location. Each row represents one neuron, sorted by soma locations in PVH subdivisions; columns represent subdivisions of PVH, and values denote dendrite lengths (μm) in each subdivision.

(J–M) Comparison of axon lengths (J), number of axon terminals (K), number of target regions (L), and number of primary dendrites (M) based on soma location in PVH subdivisions; Kruskal-Wallis test with Dunn's post hoc test.

(N) UMAP representation of all neurons (as in Figure 2O) color-coded according to soma location in PVH subdivisions.

(O–Q) Comparison of soma volumes (O), soma areas (P), and soma BoundingBoxOO lengths (Q) based on soma location in PVH subdivisions, Kruskal-Wallis test with Dunn's post hoc test.

Data are presented as mean ± SEM; *$p < 0.05$, **$p < 0.01$, ***$p < 0.001$.

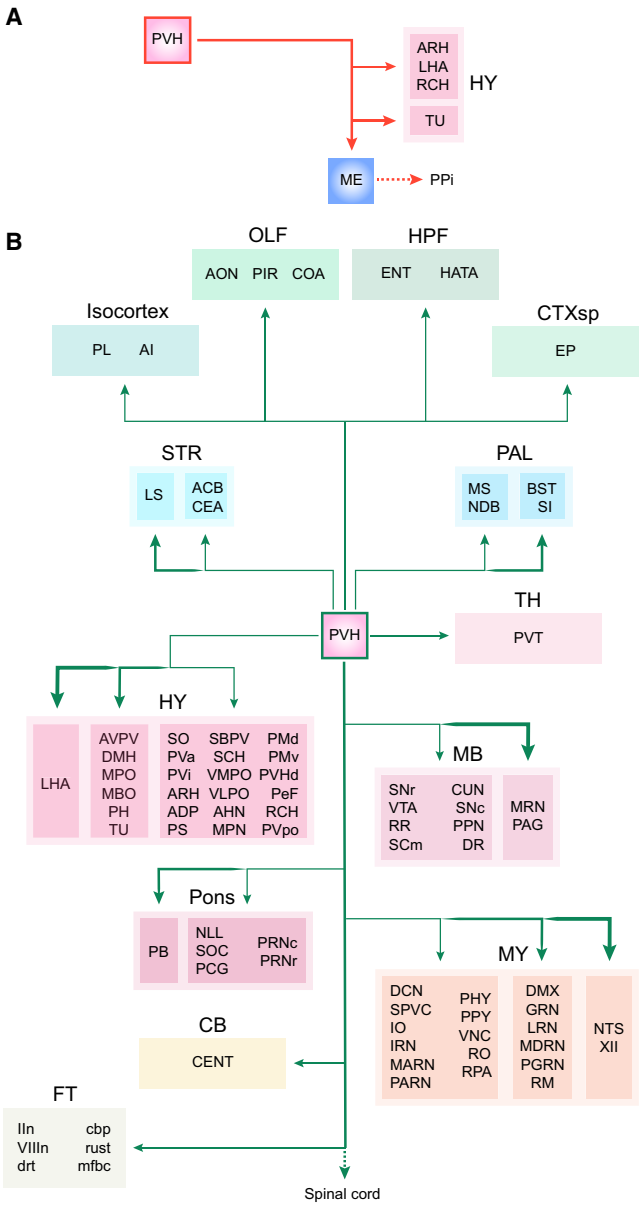

Figure 8. Wiring diagram of C1 and C2 neuron projection targets

Summary wiring diagrams of C1 (A) and C2 (B) neurons according to terminal numbers in each projection target. Boxes represent target regions color-coded by brain divisions. Target regions were ranked based on terminal number (TN). The median number (M) of total C1 and C2 neuron axon terminals in target regions were 10 and 12, respectively; target regions with terminals less than the median were not included in the wiring diagram. Line thickness represents the relative innervation strength based on terminal numbers in each target region and is defined as standard ($M \leq TN < [5 \times M]$), moderate ($[5 \times M] \leq TN < [9 \times M]$), or strong ($[9 \times M] \leq TN$). Targets based on published literature are connected using dotted line. The full list of C2 targets, including those with TN below median, is presented in Table S9.

See also Figures S6–S8 and Tables S9 and S10.

Magnocellular neurons are defined as cells that project to the PPi, whereas parvocellular neurons project to the brainstem, spinal cord,[69] ME, or anterior pituitary,[16] but not PPi. Neurons projecting to ME include those terminating in ME, as well as those projecting to the anterior and posterior lobes of pituitary,[70–73] all regions supplied by capillaries and labelable by peripheral FG injection. FG-labeled neurons have electrophysiological signatures of magnocellular OXT neurons.[27] Combining our projectome with existing knowledge, C1 neurons included all magnocellular cells (but not vice versa), whereas parvocellular cells included all C2 neurons (but not vice versa).

A major difference between our results and previous studies is the finding that ME-projecting C1 neurons do not project to the endbrain. For example, CEA, the first region shown to be innervated by PVH OXT neurons projecting to PPi,[19] negatively correlated with ME ($r = -0.115$, $p = 0.208$) in our correlation matrix (Figure S3A). Lateral septal nucleus (LS) and BST, also thought to be innervated by magnocellular PVH OXT neurons,[74] negatively and significantly correlated with ME (LS, $r = -0.196$, $p < 0.05$; BST, $r = -0.219$, $p < 0.05$). CEA, instead, had significant positive correlations with PAG, PB, and MARN, regions exclusively innervated by C2 OXT neurons. How could this apparent discrepancy be explained? We only labeled PVH OXT neurons, whereas previous retrograde labeling experiments did not specify the origin of OXT neurons. Thus, it is possible that OXT neurons from other brain regions co-projected to ME and endbrain. Dye-coupling (via somatosomatic connections and/or synaptic contacts) between OXT neurons has been extensively reported[75–77]; such coupling may also lead to co-labeling of PPi and endbrain regions. In samples labeled at higher density, arbors of adjacent cells may be difficult to untangle. Earlier in the study, when we tried to reconstruct cells from bulk labeled samples, we also thought we observed neurons co-projecting to ME and endbrain and/or midbrain regions; however, in sparsely labeled samples, none of the 177 reconstructed ME-projecting neurons had collaterals outside of the hypothalamus (Figure 4). Interestingly, dendrites of some C1 neurons extended to the thalamic regions of RE and Xi and may account for some of the extra hypothalamic fibers reported in other studies. We note that some reconstructed OXT axons in trout and rats appear to have multiple axons.[21,75]

Our C2 neuron projection patterns are consistent with previous reports of parvocellular neuron projections. For example, a recent mouse study labeling PPi-projecting PVH OXT neurons using FG, and ACB-projecting neurons using retro-beads, found that FG-labeled neurons do not project to ACB; the parvocellular characteristics of ACB-projecting neurons were confirmed using electrophysiology, providing evidence that parvocellular neurons project to the forebrain.[27] Consistently, in our correlation matrix, ACB positively correlated with MRN ($r = 0.245$, $p < 0.0001$, Figure S3A). With 79% of C2 neurons projecting to MRN, it serves as a signature target of C2 neurons; negative correlation between MRN and ME ($r = -0.641$, $p < 0.0001$) provides additional evidence for C2 neurons being parvocellular. MRN also highly correlated with NTS ($r = 0.523$, $p < 0.0001$) and SO ($r = 0.235$, $p < 0.0001$), both previously shown to be targets of parvocellular neurons.[69,78,79]

Based on our results and evidence from the published literature, a simple classification of PVH OXT neurons based on projectomes would be C1 ME-projecting neurons vs. C2 non-ME-projecting neurons, with C2 neurons covering all known projections of PVH OXT neurons outside of the hypothalamus.

Projectome and morphological characterization of C1 and C2 OXT neurons

As compared with bulk labeling, which have threshold issues, single-neuron projectomes can catch all regions covered by axon fibers, including those with few projections. In our analysis, we identified 214 regions covered by PVH OXT neurons, more than double that of previous mesoscale analysis.[17] The brain regions found to be proportionally more extensively covered in our single-neuron projectome analysis included the olfactory area, hippocampal formation, and thalamus. Cerebellum and fiber tracts projections were not reported previously. Of reported OXT targets, we only missed auditory, visual, visceral, and gustatory areas[17,80]; these regions are all covered in our mesoscale projectome. Thus, our method can label OXT neurons projecting to all known projection targets. The above-mentioned areas were missed possibly because they have relatively fewer projecting fibers; it is also not known if OXT neurons with different projection patterns are labeled with equal efficiency. We note that we traced from all brightly labeled and identifiable fibers back to the soma; thus, there was no bias for soma position or projection patterns during tracing.

In terms of correlation between soma position and projection targets, a previous work showed that peripherally injected FG mostly labeled somata in the anterior two-thirds of the PVH; retrograde dye- and bead-labeling of the DMX, NTS, and spinal cord marked somata mostly positioned in the posterior one-third of the PVH.[68] Our results also showed location of C1 neuron somata more anteriorly within the PVH than C2 neurons (Figure 2K). Random multicolor labeling of isotocin (OXT homolog) neurons in Rainbow transgenic larval zebrafish showed that axons projecting to PPi do not simultaneously project to the endbrain and brainstem, and have somata located in anterior parts of neurosecretory preoptic area (NPO); non-PPi projecting neurons innervated both forebrain and brainstem regions, and were located at the posterior of NPO.[81] Consistently, our results showed that C1 neurons projected within the hypothalamus (76% exclusively to ME, and other 24% have other projections within the hypothalamus) and have somata located to anterior parts of PVH (Figure 2). The projection patterns of non-PPi projecting isotocin neurons without endbrain projections, and non-PPi and forebrain projecting isotocin neurons, are similar to the projection patterns to C2-1 neurons and C2-2 and C2-3 neurons combined, respectively. In other words, the projection patterns of PVH OXT neuron clusters and subtypes we report highly consistent with those observed in zebrafish, suggesting conservation through evolution.

In terms of dendrite arborization, C2 neurons have more primary dendrites than C1 neurons (Figure 2L), consistent with previous classification based on electrophysiological properties[82] and projection targets[68] in mice. C2 dendrites also extended to other nuclei close to PVH; these dendrites may serve as an early interface for coordinating neuroendocrine and central regulation in response to internal and external stimuli.[68] Extensive dendrite arborization of C2 neurons within and near PVH, especially around V3 suggests that they could be an important source of CSF OXT.[5]

Projection targets and their correlations

The projection target correlation matrices of single-neuron projectomes provide rich information for dissecting and analyzing the projection patterns of OXT neurons. Here, we use the following examples to illustrate how they contribute to better understanding of OXT function, as well as potential identification of new functions.

In a first example, TU contains many terminals, evenly distributed between C1 and C2 neurons. For C1 neurons, the projection target correlation matrix of TU positively correlated with other targets including PeF, AHN, PVHd, ARH, LHA, and ME; both ARH and LHA are essential for regulating food intake. For C2 neurons, more specifically C2-2 and C2-3 neurons, in addition to projecting to the above-mentioned regions, TU-projecting neurons also co-project to VTA and RR of the dopaminergic system, as well as LS and MEA of the limbic system. Given that TU is involved in regulation of feeding by environmental context,[83] OXT neurons likely regulate basic feeding behavior through C1 neurons and contribute to modulation of feeding by environmental factors through C2 neurons.

An interesting region identified by our projection correlation analysis is ACB, which positively correlated with a total of 66 regions. PVH OXT neurons projecting to ACB have been shown to be involved in social reward, where OXT acts as a social reinforcement signal.[63] Consistent with this function, ACB, a member of the biggest correlation cluster of C2-2 projection targets, correlated positively with regions involved in olfactory information processing and memory systems, providing morphological evidence for co-regulation of these regions. Interestingly, C2-2 neuron projecting to ACB also co-projected to ARH, which is involved in food intake; this co-projection pattern has not been reported before. Given that OXT is generally thought to repress food intake, an interesting question is whether OXT-dependent food and social rewards compete. Individual C2-2 OXT neurons co-project broadly to multiple neuromodulatory centers in the brain, including those of serotoninergic, cholinergic, dopaminergic, and adrenergic neurons. These results are consistent with global or master neuroregulatory roles of C2-2 neurons.

Finally, OXT is generally thought to mediate coordinated central and peripheral neuromodulation. How is this achieved? In our reconstructions, although ME-projecting C1 neurons do not extend axons outside of the hypothalamus, there is extensive overlap between C1 and C2 dendrites. Thus, peripheral and central modulation can be coordinated through somatodendritic, dendrodendritic, and somatosomatic contacts. Furthermore, 10% of C2 neurons project to SO (3% of all neurons, consistent with previous report[79]); SO has extensive OXT projections to PPi.[16] PVH OXT neurons projecting to SO, and other regions containing OXT neurons likely contribute to crosstalk between central and peripheral neuromodulation.

Future directions

An important follow up of our study is whether subtypes we identified correlate with specific molecular identities of OXT neurons? We validated *Calb1* and *Reln* as relatively specific markers of C1 and C2 neurons, respectively (Figure 3). However, given than these genes are also expressed in non-OXT neurons, intersectional genetics would be needed to specifically label C1 or C2 neurons. A previous study[27] showed that non-FG-labeled PVH OXT neurons highly expressed genes linked to the pathogenesis of autism spectrum disorder (ASD); consistently, our results showed that C2-2 neurons have extensive projections in the brain to regions associated with social functions. Thus, it would

be interesting to generate *Oxt-ires-Cre*;*Reln-Flp* mice and use Cre- and Flp-dependent optogenetics or chemogenetics to examine whether activation of C2 neurons regulates social behaviors in wild-type mice and ASD mouse models.

Cell-type-specific tracing of the relationship between input and output (cTRIO) can also be applied to decipher subtype-specific input-output relationships, in order to better understand how PVH OXT neuronal subtypes process information. The data we present in Figure S5 and Table S9 describe the projection strength and target of subtypes of PVH OXT neurons in different brain regions. Cre- and Flp-dependent approaches can be used to label OXT neurons projecting to specific targets, chemogenetics, and optogenetics can be used to identify the specific function of subgroups of OXT neurons, and sequencing of labeled OXT neurons may generate specific markers for subtypes of OXT neurons.

Although the results presented may open more questions than they answer, our single-neuron projectomes and systematic analysis, mapped to CCFv3, provides comprehensive, searchable, and visualizable high-resolution morphological information for the broad community interested in OXT function.

STAR★METHODS

Detailed methods are provided in the online version of this paper and include the following:

- KEY RESOURCES TABLE
- RESOURCE AVAILABILITY
  - Lead contact
  - Materials availability
  - Data and code availability
- EXPERIMENTAL MODEL AND STUDY PARTICIPANT DETAILS
  - Animals
- METHOD DETAILS
  - Nomenclature and abbreviations in CCFv3 ontology of mouse brain regions mentioned in this study
  - Endbrain includes IsoCTX, OLF, HPF, CTXsp, STR and PAL
  - Interbrain includes TH and HY
  - Brainstem includes midbrain and hindbrain
  - Hindbrain includes Pons, MY and CB
- VIRAL CONSTRUCTION
- INTRAPERITONEAL AND *IN VIVO* STEREOTAXIC INJECTIONS
- IMMUNOHISTOCHEMISTRY, IMAGE ACQUISITION AND ANALYSIS
- SINGLE-MOLECULE FLUORESCENT *IN SITU* HYBRIDIZATION, IMAGE ACQUISITION AND ANALYSIS
- SINGLE-CELL PROJECTOMES: DATA ACQUISITION AND ANALYSIS
  - fMOST image collection and preprocessing
  - Single-neuron reconstruction of axons, dendrites and somata
  - fMOST image registration to CCFv3
  - Hierarchical clustering of reconstructed OXT neurons based on single-neuron projectomes
  - Correlation matrix of reconstructed axon projection strength and targets
  - Analysis of morphological features of individual neurons
  - Structure extraction of PVH and other brain regions
- MESOSCALE PROJECTOMES: DATA ACQUISITION AND ANALYSIS
  - fMOST image collection and preprocessing of bulk labeled samples
  - Mesoscale projection intensity in bulk labeling datasets
- QUANTIFICATION AND STATISTICAL ANALYSIS

SUPPLEMENTAL INFORMATION

Supplemental information can be found online at https://doi.org/10.1016/j.neuron.2023.12.022.

ACKNOWLEDGMENTS

We thank faculty, staff members, and students of HUST-Suzhou Institute for Brainsmatics, Mouse Brain Connectome Core Facility, and Big Data of Brain Atlas Facility of CEBSIT for data acquisition and preprocessing. We thank Dr. Karl Deisseroth for constructs. We thank Shajin Huang and Bei Lv for animal care and genotyping, and Dr. Le Gao for help with FNT software. We thank the Optical Imaging and Animal Facilities of CEBSIT and the National Center for Protein Sciences at Peking University for technical support. We thank members of the Yu lab and colleagues at CEBSIT and at Peking University for comments and suggestions. This work was supported by grants from the Ministry of Science and Technology of China (2021ZD0202500), the Shanghai Municipal Science and Technology Major Project (2018SHZDZX05), the Beijing Municipal Science and Technology Commission (Z210010), the Key-Area Research and Development Program of Guangdong Province (2019B030335001), the National Natural Science Foundation of China (T2122015, 61890953), and the State Key Laboratory of Membrane Biology. The funders had no role in study design, data collection and analysis, decision to publish, or preparation of the manuscript.

AUTHOR CONTRIBUTIONS

Conceptualization, H.L., Q.L., H.G., W.-J.B., A.L., and X.Y.; methodology and software, T.J., S.A., M.X., L.G., J. Yan, J. Yuan, X.X., Q.-F.W., and A.L.; investigation, H.L., W.-J.B., and M.X.; formal analysis, H.L., S.A., B.R., and W.-J.B.; validation, H.L. and X.S.; data curation, H.L. and X.W.; visualization, H.L.; writing – original draft, H.L. and X.Y.; writing – review and editing, H.L., W.-J.B., and X.Y.; project administration, T.J., H.G., A.L., and X.Y.; fund acquisition, X.Y., A.L., H.G., Q.-F.W., J. Yan, and X.X.

DECLARATION OF INTERESTS

X.Y. is a member of the advisory board of *Neuron*.

Received: April 7, 2023
Revised: November 7, 2023
Accepted: December 29, 2023
Published: January 29, 2024

REFERENCES

1. Dale, H.H. (1906). On some physiological actions of ergot. J. Physiol. *34*, 163–206.
2. Dale, H.H. (1909). The Action of Extracts of the Pituitary Body. Biochem. J. *4*, 427–447.
3. Bargmann, W., and Scharrer, E. (1951). The site of origin of the hormones of the posterior pituitary. Am. Sci. *39*, 255–259.

4. Landgraf, R., and Neumann, I.D. (2004). Vasopressin and oxytocin release within the brain: a dynamic concept of multiple and variable modes of neuropeptide communication. Front. Neuroendocrinol. *25*, 150–176.

5. Ludwig, M., and Leng, G. (2006). Dendritic peptide release and peptide-dependent behaviours. Nat. Rev. Neurosci. *7*, 126–136.

6. Veenema, A.H., and Neumann, I.D. (2008). Central vasopressin and oxytocin release: regulation of complex social behaviours. Prog. Brain Res. *170*, 261–276.

7. Sofroniew, M.V. (1980). Projections from vasopressin, oxytocin, and neurophysin neurons to neural targets in the rat and human. J. Histochem. Cytochem. *28*, 475–478.

8. Sofroniew, M.V. (1983). Morphology of vasopressin and oxytocin neurones and their central and vascular projections. Prog. Brain Res. *60*, 101–114.

9. Sofroniew, M.V., and Glasmann, W. (1981). Golgi-like immunoperoxidase staining of hypothalamic magnocellular neurons that contain vasopressin, oxytocin or neurophysin in the rat. Neuroscience *6*, 619–643.

10. Antoni, F.A. (1993). Vasopressinergic control of pituitary adrenocorticotropin secretion comes of age. Front. Neuroendocrinol. *14*, 76–122.

11. Engelmann, M., Landgraf, R., and Wotjak, C.T. (2004). The hypothalamic-neurohypophysial system regulates the hypothalamic-pituitary-adrenal axis under stress: an old concept revisited. Front. Neuroendocrinol. *25*, 132–149.

12. Rodríguez, E.M., Blázquez, J.L., and Guerra, M. (2010). The design of barriers in the hypothalamus allows the median eminence and the arcuate nucleus to enjoy private milieus: the former opens to the portal blood and the latter to the cerebrospinal fluid. Peptides *31*, 757–776.

13. Gimpl, G., and Fahrenholz, F. (2001). The Oxytocin Receptor System: Structure, function, and regulation. Physiol. Rev. *81*, 629–683.

14. Viero, C., Shibuya, I., Kitamura, N., Verkhratsky, A., Fujihara, H., Katoh, A., Ueta, Y., Zingg, H.H., Chvatal, A., Sykova, E., et al. (2010). REVIEW: Oxytocin: Crossing the bridge between basic science and pharmacotherapy. CNS Neurosci. Ther. *16*, e138–e156.

15. Jurek, B., and Neumann, I.D. (2018). The Oxytocin Receptor: From Intracellular Signaling to Behavior. Physiol. Rev. *98*, 1805–1908.

16. Swanson, L.W., and Sawchenko, P.E. (1983). Hypothalamic integration: organization of the paraventricular and supraoptic nuclei. Annu. Rev. Neurosci. *6*, 269–324.

17. Son, S., Manjila, S.B., Newmaster, K.T., Wu, Y.T., Vanselow, D.J., Ciarletta, M., Anthony, T.E., Cheng, K.C., and Kim, Y. (2022). Whole-Brain Wiring Diagram of Oxytocin System in Adult Mice. J. Neurosci. *42*, 5021–5033.

18. Swanson, L.W. (1977). Immunohistochemical evidence for a neurophysin-containing autonomic pathway arising in the paraventricular nucleus of the hypothalamus. Brain Res. *128*, 346–353.

19. Knobloch, H.S., Charlet, A., Hoffmann, L.C., Eliava, M., Khrulev, S., Cetin, A.H., Osten, P., Schwarz, M.K., Seeburg, P.H., Stoop, R., et al. (2012). Evoked axonal oxytocin release in the central amygdala attenuates fear response. Neuron *73*, 553–566.

20. Ross, H.E., Cole, C.D., Smith, Y., Neumann, I.D., Landgraf, R., Murphy, A.Z., and Young, L.J. (2009). Characterization of the oxytocin system regulating affiliative behavior in female prairie voles. Neuroscience *162*, 892–903.

21. Zhang, B., Qiu, L., Xiao, W., Ni, H., Chen, L., Wang, F., Mai, W., Wu, J., Bao, A., Hu, H., et al. (2021). Reconstruction of the Hypothalamo-Neurohypophysial System and Functional Dissection of Magnocellular Oxytocin Neurons in the Brain. Neuron *109*, 331–346.e7.

22. Shaner, N.C., Patterson, G.H., and Davidson, M.W. (2007). Advances in fluorescent protein technology. J. Cell Sci. *120*, 4247–4260.

23. Gong, H., Xu, D., Yuan, J., Li, X., Guo, C., Peng, J., Li, Y., Schwarz, L.A., Li, A., Hu, B., et al. (2016). High-throughput dual-colour precision imaging for brain-wide connectome with cytoarchitectonic landmarks at the cellular level. Nat. Commun. *7*, 12142.

24. Zhong, Q., Li, A., Jin, R., Zhang, D., Li, X., Jia, X., Ding, Z., Luo, P., Zhou, C., Jiang, C., et al. (2021). High-definition imaging using line-illumination modulation microscopy. Nat. Methods *18*, 309–315.

25. Gao, L., Liu, S., Gou, L., Hu, Y., Liu, Y., Deng, L., Ma, D., Wang, H., Yang, Q., Chen, Z., et al. (2022). Single-neuron projectome of mouse prefrontal cortex. Nat. Neurosci. *25*, 515–529.

26. Charrad, M., Ghazzali, N., Boiteau, V., and Niknafs, A. (2014). NbClust: An R Package for Determining the Relevant Number of Clusters in a Data Set. J. Stat. Softw. *61*, 1–36.

27. Lewis, E.M., Stein-O'Brien, G.L., Patino, A.V., Nardou, R., Grossman, C.D., Brown, M., Bangamwabo, B., Ndiaye, N., Giovinazzo, D., Dardani, I., et al. (2020). Parallel Social Information Processing Circuits Are Differentially Impacted in Autism. Neuron *108*, 659–675.e6.

28. Luther, J.A., and Tasker, J.G. (2000). Voltage-gated currents distinguish parvocellular from magnocellular neurones in the rat hypothalamic paraventricular nucleus. J. Physiol. *523*, 193–209.

29. Choi, H.M.T., Schwarzkopf, M., Fornace, M.E., Acharya, A., Artavanis, G., Stegmaier, J., Cunha, A., and Pierce, N.A. (2018). Third-generation in situ hybridization chain reaction: multiplexed, quantitative, sensitive, versatile, robust. Development *145*, dev165753.

30. Leng, G., and Ludwig, M. (2008). Neurotransmitters and peptides: whispered secrets and public announcements. J. Physiol. *586*, 5625–5632.

31. Cipolla-Neto, J., Skorupa, A.L., Ribeiro-Barbosa, E.R., Bartol, I., Mota, S.R., Afeche, S.C., Delagrange, P., Guardiola-Lemaitre, B., and Canteras, N.S. (1999). The role of the retrochiasmatic area in the control of pineal metabolism. Neuroendocrinology *69*, 97–104.

32. Simpson, K.A., Martin, N.M., and Bloom, S.R. (2009). Hypothalamic regulation of food intake and clinical therapeutic applications. Arq. Bras. Endocrinol. Metabol. *53*, 120–128.

33. Siegel, J.M. (1979). Behavioral functions of the reticular formation. Brain Res. *180*, 69–105.

34. Cowley, K.C. (2005). Psychogenic and pharmacologic induction of the let-down reflex can facilitate breastfeeding by tetraplegic women: A report of 3 cases. Arch. Phys. Med. Rehabil. *86*, 1261–1264.

35. Swanson, L.W. (2000). Cerebral hemisphere regulation of motivated behavior. Brain Res. *886*, 113–164.

36. Kalra, S.P., and Kalra, P.S. (2004). Hypothalamic Regulation of Appetite and Obesity. In Encyclopedia of Endocrine Diseases, L. Martini, ed. (Elsevier), pp. 699–706.

37. Swanson, L.W., and Sawchenko, P.E. (1980). Paraventricular nucleus: a site for the integration of neuroendocrine and autonomic mechanisms. Neuroendocrinology *31*, 410–417.

38. Wang, J.W., Lundeberg, T., and Yu, L.C. (2003). Antinociceptive role of oxytocin in the nucleus raphe magnus of rats, an involvement of μ-opioid receptor. Regul. Pept. *115*, 153–159.

39. Syka, J. (2010). Subcortical responses to species-specific vocalizations. Chapter 4.1. In Handbook of Behavioral Neuroscience, S.M. Brudzynski, ed. (Elsevier), pp. 99–112.

40. Michelsen, K.A., Prickaerts, J., and Steinbusch, H.W. (2008). The dorsal raphe nucleus and serotonin: implications for neuroplasticity linked to major depression and Alzheimer's disease. Prog. Brain Res. *172*, 233–264.

41. Zhang, X. (2007). Spinohypothalamic Tract, Anatomical Organization and Response Properties. In Encyclopedia of Pain, R.F. Schmidt and W.D. Willis, eds. (Springer), pp. 2251–2253.

42. Febo, M., Shields, J., Ferris, C.F., and King, J.A. (2009). Oxytocin modulates unconditioned fear response in lactating dams: an fMRI study. Brain Res. *1302*, 183–193.

43. Bhattarai, J.P., Etyemez, S., Jaaro-Peled, H., Janke, E., Leon Tolosa, U.D., Kamiya, A., Gottfried, J.A., Sawa, A., and Ma, M. (2022). Olfactory modulation of the medial prefrontal cortex circuitry: Implications for social cognition. Semin. Cell Dev. Biol. *129*, 31–39.

44. Treede, R.D., Kenshalo, D.R., Gracely, R.H., and Jones, A.K. (1999). The cortical representation of pain. Pain *79*, 105–111.

45. Vierck, C.J., Whitsel, B.L., Favorov, O.V., Brown, A.W., and Tommerdahl, M. (2013). Role of primary somatosensory cortex in the coding of pain. Pain *154*, 334–344.

46. Genaro, K., and Prado, W.A. (2021). The role of the anterior pretectal nucleus in pain modulation: A comprehensive review. Published online April 28, 2021. Eur. J. Neurosci.

47. Gamer, M., Zurowski, B., and Büchel, C. (2010). Different amygdala subregions mediate valence-related and attentional effects of oxytocin in humans. Proc. Natl. Acad. Sci. USA *107*, 9400–9405.

48. Dobolyi, A., Cservenák, M., and Young, L.J. (2018). Thalamic integration of social stimuli regulating parental behavior and the oxytocin system. Front. Neuroendocrinol. *51*, 102–115.

49. Yasui, Y., Nakano, K., and Mizuno, N. (1992). Descending projections from the subparafascicular thalamic nucleus to the lower brain stem in the rat. Exp. Brain Res. *90*, 508–518.

50. Horn, A.K.E. (2006). The reticular formation. In Progress in Brain Research, J.A. Büttner-Ennever, ed. (Elsevier), pp. 127–155.

51. Gauriau, C., and Bernard, J.F. (2002). Pain pathways and parabrachial circuits in the rat. Exp. Physiol. *87*, 251–258.

52. Toor, R.U.A.S., Sun, Q.J., Kumar, N.N., Le, S., Hildreth, C.M., Phillips, J.K., and McMullan, S. (2019). Neurons in the Intermediate Reticular Nucleus Coordinate Postinspiratory Activity, Swallowing, and Respiratory-Sympathetic Coupling in the Rat. J. Neurosci. *39*, 9757–9766.

53. Myers, B., and Greenwood-Van Meerveld, B. (2009). Role of anxiety in the pathophysiology of irritable bowel syndrome: importance of the amygdala. Front. Neurosci. *3*, 47.

54. Garcia-Rill, E. (2019). Arousal and movement disorders. In Arousal in Neurological and Psychiatric Diseases (Springer), pp. 179–193.

55. Gastard, M., Jensen, S.L., Martin, J.R., Williams, E.A., and Zahm, D.S. (2002). The caudal sublenticular region/anterior amygdaloid area is the only part of the rat forebrain and mesopontine tegmentum occupied by magnocellular cholinergic neurons that receives outputs from the central division of extended amygdala. Brain Res. *957*, 207–222.

56. Adams, D.B. (1979). Brain mechanisms for offense, defense, and submission. Behav. Brain Sci. *2*, 201–213.

57. Steriade, M., and Llinás, R.R. (1988). The functional states of the thalamus and the associated neuronal interplay. Physiol. Rev. *68*, 649–742.

58. Arts, M.P., Bemelmans, F.F., and Cools, A.R. (1998). Role of the retrorubral nucleus in striatally elicited orofacial dyskinesia in cats: effects of muscimol and bicuculline. Psychopharmacology *140*, 150–156.

59. Wheatcroft, T., Saleem, A.B., and Solomon, S.G. (2022). Functional Organisation of the Mouse Superior Colliculus. Front. Neural Circuits *16*, 792959.

60. Soiza-Reilly, M., and Gaspar, P. (2020). From B1 to B9: a guide through hindbrain serotonin neurons with additional views from multidimensional characterization. Chapter 2. In Handbook of Behavioral Neuroscience, C.P. Müller and K.A. Cunningham, eds. (Elsevier), pp. 23–40.

61. Li, X., Yu, B., Sun, Q., Zhang, Y., Ren, M., Zhang, X., Li, A., Yuan, J., Madisen, L., Luo, Q., et al. (2018). Generation of a whole-brain atlas for the cholinergic system and mesoscopic projectome analysis of basal forebrain cholinergic neurons. Proc. Natl. Acad. Sci. USA *115*, 415–420.

62. Lévy, F., Kendrick, K.M., Goode, J.A., Guevara-Guzman, R., and Keverne, E.B. (1995). Oxytocin and vasopressin release in the olfactory bulb of parturient ewes: changes with maternal experience and effects on acetylcholine, γ-aminobutyric acid, glutamate and noradrenaline release. Brain Res. *669*, 197–206.

63. Dölen, G., Darvishzadeh, A., Huang, K.W., and Malenka, R.C. (2013). Social reward requires coordinated activity of nucleus accumbens oxytocin and serotonin. Nature *501*, 179–184.

64. Hung, L.W., Neuner, S., Polepalli, J.S., Beier, K.T., Wright, M., Walsh, J.J., Lewis, E.M., Luo, L., Deisseroth, K., Dölen, G., et al. (2017). Gating of social reward by oxytocin in the ventral tegmental area. Science *357*, 1406–1411.

65. Xiao, L., Priest, M.F., Nasenbeny, J., Lu, T., and Kozorovitskiy, Y. (2017). Biased Oxytocinergic Modulation of Midbrain Dopamine Systems. Neuron *95*, 368–384.e5.

66. Liu, Y., Shan, L., Liu, T., Li, J., Chen, Y., Sun, C., Yang, C., Bian, X., Niu, Y., Zhang, C., et al. (2023). Molecular and cellular mechanisms of the first social relationship: A conserved role of 5-HT from mice to monkeys, upstream of oxytocin. Neuron *111*, 1468–1485.e7.

67. Chini, B., Verhage, M., and Grinevich, V. (2017). The Action Radius of Oxytocin Release in the Mammalian CNS: From Single Vesicles to Behavior. Trends Pharmacol. Sci. *38*, 982–991.

68. Biag, J., Huang, Y., Gou, L., Hintiryan, H., Askarinam, A., Hahn, J.D., Toga, A.W., and Dong, H.W. (2012). Cyto- and chemoarchitecture of the hypothalamic paraventricular nucleus in the C57BL/6J male mouse: a study of immunostaining and multiple fluorescent tract tracing. J. Comp. Neurol. *520*, 6–33.

69. Hosoya, Y., and Matsushita, M. (1979). Identification and distribution of the spinal and hypophyseal projection neurons in the paraventricular nucleus of the rat. A light and electron microscopic study with the horseradish peroxidase method. Exp. Brain Res. *35*, 315–331.

70. Horn, A.M., Robinson, I.C., and Fink, G. (1985). Oxytocin and vasopressin in rat hypophysial portal blood: experimental studies in normal and Brattleboro rats. J. Endocrinol. *104*, 211–224.

71. Sheward, W.J., Coombes, J.E., Bicknell, R.J., Fink, G., and Russell, J.A. (1990). Release of oxytocin but not corticotrophin-releasing factor-41 into rat hypophysial portal vessel blood can be made opiate dependent. J. Endocrinol. *124*, 141–150.

72. Denef, C. (2008). Paracrinicity: the story of 30 years of cellular pituitary crosstalk. J. Neuroendocrinol. *20*, 1–70.

73. Knobloch, H.S., and Grinevich, V. (2014). Evolution of oxytocin pathways in the brain of vertebrates. Front. Behav. Neurosci. *8*, 31.

74. Althammer, F., and Grinevich, V. (2017). Diversity of oxytocin neurons: beyond magno- and parvocellular cell types?. Published online October 12, 2017. J. Neuroendocrinol..

75. Saito, D., Komatsuda, M., and Urano, A. (2004). Functional organization of preoptic vasotocin and isotocin neurons in the brain of rainbow trout: central and neurohypophysial projections of single neurons. Neuroscience *124*, 973–984.

76. Tweedle, C.D., and Hatton, G.I. (1976). Ultrastructural comparisons of neurons of supraoptic and circularis nuclei in normal and dehydrated rats. Brain Res. Bull. *1*, 103–121.

77. van den Pol, A.N. (1982). The magnocellular and parvocellular paraventricular nucleus of rat: intrinsic organization. J. Comp. Neurol. *206*, 317–345.

78. Swanson, L.W., and Kuypers, H.G. (1980). The paraventricular nucleus of the hypothalamus: cytoarchitectonic subdivisions and organization of projections to the pituitary, dorsal vagal complex, and spinal cord as demonstrated by retrograde fluorescence double-labeling methods. J. Comp. Neurol. *194*, 555–570.

79. Eliava, M., Melchior, M., Knobloch-Bollmann, H.S., Wahis, J., da Silva Gouveia, M., Tang, Y., Ciobanu, A.C., Triana Del Rio, R., Roth, L.C., Althammer, F., et al. (2016). A New Population of Parvocellular Oxytocin Neurons Controlling Magnocellular Neuron Activity and Inflammatory Pain Processing. Neuron *89*, 1291–1304.

80. Marlin, B.J., Mitre, M., D'amour, J.A., Chao, M.V., and Froemke, R.C. (2015). Oxytocin enables maternal behaviour by balancing cortical inhibition. Nature *520*, 499–504.

81. Herget, U., Gutierrez-Triana, J.A., Salazar Thula, O., Knerr, B., and Ryu, S. (2017). Single-Cell Reconstruction of Oxytocinergic Neurons Reveals Separate Hypophysiotropic and Encephalotropic Subtypes in Larval Zebrafish. eNeuro *4*. ENEURO.0278-16.2016.

82. Chen, S., Xu, H., Dong, S., and Xiao, L. (2022). Morpho-Electric Properties and Diversity of Oxytocin Neurons in Paraventricular Nucleus of Hypothalamus in Female and Male Mice. J. Neurosci. *42*, 2885–2904.

83. Mohammad, H., Senol, E., Graf, M., Lee, C.Y., Li, Q., Liu, Q., Yeo, X.Y., Wang, M.H., Laskaratos, A., Xu, F.Q., et al. (2021). A neural circuit for excessive feeding driven by environmental context in mice. Nat. Neurosci. *24*, 1132–1141.

84. Wu, Z., Xu, Y., Zhu, Y., Sutton, A.K., Zhao, R., Lowell, B.B., Olson, D.P., and Tong, Q. (2012). An obligate role of oxytocin neurons in diet induced energy expenditure. PLoS One *7*, e45167.

85. Nguyen, A.W., and Daugherty, P.S. (2005). Evolutionary optimization of fluorescent proteins for intracellular FRET. Nat. Biotechnol. *23*, 355–360.

86. Zacharias, D.A., Violin, J.D., Newton, A.C., and Tsien, R.Y. (2002). Partitioning of lipid-modified monomeric GFPs into membrane microdomains of live cells. Science *296*, 913–916.

87. Patriarchi, T., Cho, J.R., Merten, K., Howe, M.W., Marley, A., Xiong, W.H., Folk, R.W., Broussard, G.J., Liang, R., Jang, M.J., et al. (2018). Ultrafast neuronal imaging of dopamine dynamics with designed genetically encoded sensors. Science *360*, eaat4422.

88. Ni, H., Tan, C., Feng, Z., Chen, S., Zhang, Z., Li, W., Guan, Y., Gong, H., Luo, Q., and Li, A. (2020). A Robust Image Registration Interface for Large Volume Brain Atlas. Sci. Rep. *10*, 2139.

89. Lance, G.N., and Williams, W.T. (1966). Computer Programs for Hierarchical Polythetic Classification ("Similarity Analyses"). Comput. J. *9*, 60–64.

90. Lance, G.N., and Williams, W.T. (1967). Mixed-Data Classificatory Programs I - Agglomerative Systems. Aust. Comput. J. *1*, 15–20.

91. McInnes, L., Healy, J., and Melville, J. (2018). UMAP: Uniform Manifold Approximation and Projection for Dimension Reduction. Preprint at arXiv.

STAR★METHODS

KEY RESOURCES TABLE

REAGENT or RESOURCE	SOURCE	IDENTIFIER
Antibodies		
IHC: Oxytocin	Phoenix Pharmaceuticals	Cat# H-051-01; RRID: AB_2876858
IHC: Donkey anti-Rabbit Alexa Fluor 568	Thermo Fisher Scientific	Cat# A10042; RRID: AB_2534017
Bacterial and virus strains		
rAAV (2/9)-EF1α-DIO-YPet-p2A-mGFP	BrainVTA, Wuhan	Cat# PT-0593
Chemicals, peptides, and recombinant proteins		
DAPI	Thermo Fisher Scientific	Cat# D1306, RRID: AB_2629482
Alexa Fluor 555 conjugate	Invitrogen	Cat# C34776
FluoroGold	Biorigin, Beijing	Cat# BN14040
Deposited data		
Single-neuron projectomes of PVH OXT neurons	This paper	https://doi.org/10.12412/BSDC.1704691586.20001
Experimental models: Organisms/strains		
Mouse: Oxt-ires-Cre (Oxytocin-Ires-Cre); full name: B6;129S-Oxt$^{tm1.1(cre)Dolsn}$/J	The Jackson Laboratory	RRID:IMSR_JAX: 024234
Recombinant DNA		
rAAV-EF1α-DIO-YPet-p2A-mGFP	This paper	N/A
Software and algorithms		
FNT	Gao et al.[25]	https://zenodo.org/record/5981001
Amira 5	Thermo Fisher Scientific	https://www.thermofisher.com/us/en/home/industrial/electron microscopy/electron-microscopyinstruments-workflow-solutions/3d-visualizationanalysis-software/amira-life-sciencesbiomedical.html
Imaris 9	Oxford Instruments	https://imaris.oxinst.com/
HCRprobe	Patriarchi et al.[87]	https://github.com/GradinaruLab/HCRprobe
R	R	http://www.r-project.org/
GraphPad Prism 8	GraphPad Software	https://www.graphpad.com/scientificsoftware/prism/
FIJI	NIH	https://imagej.nih.gov/ij/ RRID: SCR_003070
Matlab R2019a	MathWork	https://www.mathworks.com/
Custom Matlab code	This paper	Zenodo: https://doi.org/10.5281/zenodo.10427135
Adobe Photoshop CC 2016	Adobe	https://www.adobe.com/products/photoshop.html

RESOURCE AVAILABILITY

Lead contact

Further information and requests for resources and reagents should be directed to and will be fulfilled by the lead contact, Xiang Yu (yuxiang01@pku.edu.cn).

Materials availability

All unique reagents generated in this study are available from the lead contact upon request.

Data and code availability

- All single-cell projectome data can be publicly visualized at the website https://mouse.digital-brain.cn/projectome/pvh_oxt. The DOI for downloading the dataset is listed in the key resources table.
- Original Matlab code for analysis of mesoscale projection intensity has been deposited at Zenodo and is publicly available as of the date of publication. The DOI is listed in the key resources table.

- Any additional information required to reanalyze the data reported in this work paper is available from the lead contact upon request.

EXPERIMENTAL MODEL AND STUDY PARTICIPANT DETAILS

Animals

All animal procedures complied with the animal care standards set forth by the US National Institutes of Health and were approved by the Institutional Animal Care and Use Committee of CEBSIT, Chinese Academy of Sciences, and of Peking University. Mice were kept on C57BL/6 background and housed in cages containing corn bedding under a 12 h-12 h light-dark cycle with food and water provided ad libitum from the cage lid.

Adult C57BL6/J wildtype and *Oxt-ires-Cre* (*Oxytocin-Ires-Cre*; B6;129S-*Oxt*$^{tm1.1(cre)Dolsn}$/J; JAX stock #024234)[84] mice were used. Mice were injected with viruses, FluoroGold (FG) and/or cholera toxin subunit B (CTB) at P30 and perfused for imaging 4 weeks (sparse samples) or 8 weeks later (bulk samples), or for *in situ* hybridization 7 days later. Both males and females were used. For the lactating female group, mice were perfused 14 days after delivery.

METHOD DETAILS

Nomenclature and abbreviations in CCFv3 ontology of mouse brain regions mentioned in this study

Forebrain includes endbrain and interbrain

Endbrain includes IsoCTX, OLF, HPF, CTXsp, STR and PAL

Isocortex (IsoCTX): frontal pole, cerebral cortex (FRP), somatomotor areas (MO), somatosensory areas (SS), anterior cingulate area (ACA), prelimbic area (PL), infralimbic area (ILA), orbital area (ORB), agranular insular area (AI), retrosplenial area (RSP).

Olfactory areas (OLF): main olfactory bulb (MOB), accessory olfactory bulb (AOB), anterior olfactory nucleus (AON), taenia tecta (TT), dorsal peduncular area (DP), piriform area (PIR), nucleus of the lateral olfactory tract (NLOT), cortical amygdalar area (COA), piriform-amygdalar area (PAA), postpiriform transition area (TR).

Hippocampal formation (HPF): field CA1 (CA1), field CA2 (CA2), field CA3 (CA3), dentate gyrus (DG), entorhinal area (ENT), parasubiculum (PAR), postsubiculum (POST), presubiculum (PRE), prosubiculum (ProS), hippocampo-amygdalar transition area (HATA), area prostriata (Apr).

Cortical subplate (CTXsp): claustrum (CLA), endopiriform nucleus (EP), basolateral amygdalar nucleus (BLA), basomedial amygdalar nucleus (BMA), posterior amygdalar nucleus (PA).

Striatum (STR): caudoputamen (CP), nucleus accumbens (ACB), olfactory tubercle (OT), fundus of striatum (FS), lateral septal nucleus (LS), septofimbrial nucleus (SF), anterior amygdalar area (AAA), central amygdalar nucleus (CEA), medial amygdalar nucleus (MEA).

Pallidum (PAL): globus pallidus, external segment (GPe), globus pallidus, internal segment (GPi), magnocellular nucleus (MA), substantia innominata (SI), triangular nucleus of septum (TRS), medial septal nucleus (MS), diagonal band nucleus (NDB), bed nuclei of the stria terminalis (BST).

Interbrain includes TH and HY

Thalamus (TH): ventral medial nucleus of the thalamus (VM), ventral posterior complex of the thalamus (VP), posterior triangular thalamic nucleus (PoT), subparafascicular nucleus, magnocellular part (SPFm), subparafascicular nucleus, parvicellular part (SPFp), subparafascicular area (SPA), peripeduncular nucleus (PP), medial geniculate complex (MG), lateral posterior nucleus of the thalamus (LP), posterior limiting nucleus of the thalamus (POL), suprageniculate nucleus (SGN), ethmoid nucleus of the thalamus (Eth), interanteromedial nucleus of the thalamus (IAM), intermediodorsal nucleus of the thalamus (IMD), mediodorsal nucleus of thalamus (MD), submedial nucleus of the thalamus (SMT), perireunensis nucleus (PR), paraventricular nucleus of the thalamus (PVT), parataenial nucleus (PT), nucleus of reuniens (RE), xiphoid thalamic nucleus (Xi), rhomboid nucleus (RH), central medial nucleus of the thalamus (CM), parafascicular nucleus (PF), posterior intralaminar thalamic nucleus (PIL), reticular nucleus of the thalamus (RT), intermediate geniculate nucleus (IntG), subgeniculate nucleus (SubG), medial habenula (MH), lateral habenula (LH).

Hypothalamus (HY): supraoptic nucleus (SO), accessory supraoptic group (ASO), paraventricular hypothalamic nucleus (PVH), paraventricular hypothalamic nucleus, magnocellular division, medial magnocellular part (PVHmm), paraventricular hypothalamic nucleus, magnocellular division, posterior magnocellular part, lateral zone (PVHpml), paraventricular hypothalamic nucleus, magnocellular division, posterior magnocellular part, medial zone (PVHpmm), paraventricular hypothalamic nucleus, parvicellular division, anterior parvicellular part (PVHap), paraventricular hypothalamic nucleus, parvicellular division, medial parvicellular part, dorsal zone (PVHmpd), paraventricular hypothalamic nucleus, parvicellular division, periventricular part (PVHpv), periventricular hypothalamic nucleus, anterior part (PVa), periventricular hypothalamic nucleus, intermediate part (PVi), arcuate hypothalamic nucleus (ARH), anterodorsal preoptic nucleus (ADP), anteroventral preoptic nucleus (AVP), anteroventral periventricular nucleus (AVPV), dorsomedial nucleus of the hypothalamus (DMH), median preoptic nucleus (MEPO), medial preoptic area (MPO), vascular organ of the lamina

terminalis (OV), posterodorsal preoptic nucleus (PD), parastrial nucleus (PS), periventricular hypothalamic nucleus, posterior part (PVp), periventricular hypothalamic nucleus, preoptic part (PVpo), subparaventricular zone (SBPV), suprachiasmatic nucleus (SCH), ventromedial preoptic nucleus (VMPO), ventrolateral preoptic nucleus (VLPO), anterior hypothalamic nucleus (AHN), mammillary body (MBO), medial preoptic nucleus (MPN), dorsal premammillary nucleus (PMd), ventral premammillary nucleus (PMv), paraventricular hypothalamic nucleus, descending division (PVHd), ventromedial hypothalamic nucleus (VMH), posterior hypothalamic nucleus (PH), lateral hypothalamic area (LHA), lateral preoptic area (LPO), preparasubthalamic nucleus (PST), parasubthalamic nucleus (PSTN), perifornical nucleus (PeF), retrochiasmatic area (RCH), subthalamic nucleus (STN), tuberal nucleus (TU), zona incerta (ZI), median eminence (ME).

Brainstem includes midbrain and hindbrain

Midbrain (MB): inferior colliculus (IC), nucleus of the brachium of the inferior colliculus (NB), nucleus sagulum (SAG), parabigeminal nucleus (PBG), midbrain trigeminal nucleus (MEV), substantia nigra, reticular part (SNr), ventral tegmental area (VTA), midbrain reticular nucleus, retrorubral area (RR), midbrain reticular nucleus (MRN), superior colliculus, motor related (SCm), periaqueductal gray (PAG), pretectal region (PRT), cuneiform nucleus (CUN), red nucleus (RN), paratrochlear nucleus (Pa4), medial terminal nucleus of the accessory optic tract (MT), substantia nigra, compact part (SNc), pedunculopontine nucleus (PPN), interfascicular nucleus raphe (IF), rostral linear nucleus raphe (RL), central linear nucleus raphe (CLI), dorsal nucleus raphe (DR).

Hindbrain includes Pons, MY and CB

Pons: nucleus of the lateral lemniscus (NLL), principal sensory nucleus of the trigeminal (PSV), parabrachial nucleus (PB), superior olivary complex (SOC), Barrington's nucleus (B), pontine central gray (PCG), pontine gray (PG), pontine reticular nucleus, caudal part (PRNc), supragenual nucleus (SG), supratrigeminal nucleus (SUT), motor nucleus of trigeminal (V), peritrigeminal zone (P5), parvicellular motor 5 nucleus (PC5), locus ceruleus (LC), laterodorsal tegmental nucleus (LDT), pontine reticular nucleus (PRNr), nucleus raphe pontis (RPO), subceruleus nucleus (SLC), sublaterodorsal nucleus (SLD).

Medulla (MY): area postrema (AP), dorsal column nuclei (DCN), external cuneate nucleus (ECU), nucleus of the trapezoid body (NTB), nucleus of the solitary tract (NTS), spinal nucleus of the trigeminal, caudal part (SPVC), spinal nucleus of the trigeminal, interpolar part (SPVI), spinal nucleus of the trigeminal, oral part (SPVO), paratrigeminal nucleus (Pa5), facial motor nucleus (VII), nucleus ambiguus (AMB), dorsal motor nucleus of the vagus nerve (DMX), gigantocellular reticular nucleus (GRN), inferior olivary complex (IO), intermediate reticular nucleus (IRN), linear nucleus of the medulla (LIN), lateral reticular nucleus (LRN), magnocellular reticular nucleus (MARN), medullary reticular nucleus (MDRN), parvicellular reticular nucleus (PARN), parasolitary nucleus (PAS), paragigantocellular reticular nucleus (PGRN), perihypoglossal nuclei (PHY), parapyramidal nucleus (PPY), vestibular nuclei (VNC), nucleus x (x), hypoglossal nucleus (XII), nucleus raphe magnus (RM), nucleus raphe obscurus (RO), nucleus raphe pallidus (RPA).

Cerebellum (CB): lingula (I) (LING), central lobule (CENT), fastigial nucleus (FN), vestibulocerebellar nucleus (VeCB).

Fiber tracts (FT): olfactory nerve (In), optic nerve (IIn), oculomotor nerve (IIIn), trochlear nerve (IVn), trigeminal nerve (Vn), facial nerve (VIIn), vestibulocochlear nerve (VIIIn), vagus nerve (Xn), dorsal roots (drt), cerebellar peduncles (cbp), arbor vitae (arb), corpus callosum (cc), corticospinal tract (cst), cerebral nuclei related extrapyramidal fiber systems (epsc), tectospinal pathway (tsp), rubrospinal tract (rust), cerebrum related medial forebrain bundle system (mfbc), hypothalamus related medial forebrain bundle system (mfsbshy).

Ventricular systems: lateral ventricle (VL), third ventricle (V3), cerebral aqueduct (AQ), fourth ventricle (V4).

VIRAL CONSTRUCTION

To label the complete neuronal morphology of OXT neurons, a Cre-dependent fluorescent marker that is bright and photostable is required. After several tries, we generated pAAV-EF1α-DIO-YPet-p2A-mGFP, which fulfilled the above criteria. The sequence of yellow fluorescent protein for energy transfer (YPet)[85] was cloned in frame with p2A-mGFP (membrane-associated green fluorescent protein), which enables clear labeling of axon terminals,[86] into the pAAV-EF1α-DIO-EYFP-WPRE vector (construct gift from Karl Deisseroth, Addgene plasmid 20296) to generate pAAV-EF1α-DIO-YPet-p2A-mGFP-WPRE. Packaging of adeno-associated virus (rAAV) (Serotype 2/9) was carried out by BrainVTA, Wuhan, China (Cat# PT-0593; titer: 2.82×10^{12} transducing units (TU)/ml).

INTRAPERITONEAL AND *IN VIVO* STEREOTAXIC INJECTIONS

For labeling posterior pituitary projecting C1 neurons, 4% FluoroGold (Biorigin, Cat# BN14040) diluted in 200 μl sterile saline were intraperitoneally injected.

For *in vivo* stereotaxic injections, mice were deeply anaesthetized with 0.14 g/kg pentobarbital sodium. Viruses were injected unilaterally into the PVH (bregma: −0.8 mm; lateral: −0.65 mm; ventral: 4.3 mm) of *Oxt-ires-Cre* mice using a digital stereotaxic instrument (RWD Instruments, China). For sparse labeling of neurons, a microfluidic air pump was used to inject ultra-small and precise flows of 10 nl (original titer) rAAV (2/9)-EF1α-DIO-YPet-p2A-mGFP into PVH of *Oxt-ires-Cre* at 10 nl/min. For bulk labeling of neurons, 300 nl of rAAV (2/9)-EF1α-DIO-YPet-p2A-mGFP was injected into the PVH of virgin female, lactating female and male *Oxt-ires-Cre* mice at 70 nl/min, using a syringe pump (Harvard Apparatus). This dose labels nearly all PVH OXT neurons on the injection side,

without labeling SO neurons. To label NTS projecting C2 neurons, 200 nl CTB (1.0 mg/ml, Alexa Fluor 555 conjugate, Invitrogen, Cat# C34776) was injected bilaterally into NTS (bregma: −7.80 mm; lateral: −0.33 mm; ventral: 3.5 mm) at 20 nl/min using a syringe pump (Harvard Apparatus).

IMMUNOHISTOCHEMISTRY, IMAGE ACQUISITION AND ANALYSIS

Immunohistochemistry was carried out to ensure infection specificity. Mice were deeply anaesthetized with 0.14 g/kg pentobarbital sodium. Intracardial perfusion was performed using phosphate-buffered saline (PBS) followed by 4% paraformaldehyde (PFA). 40 μm coronal brain sections were cut using a freezing microtome (Thermo). Sections were blocked in PBS containing 5% bovine serum albumin and 0.5% Triton X-100 for 2 h at 37 °C, followed by incubation with OXT antibody (1: 500, Phoenix Pharmaceutics, Cat# H-051-01, RRID: AB_2876858) at 4 °C for 48 h. After three washes, sections were incubated with Donkey anti-Rabbit Alexa Fluor 568 secondary antibodies (Thermo Fisher Scientific, Cat# A10042, RRID: AB_2534017) at 1: 500 for 2 h at 37 °C. After another three washes, sections were incubated with DAPI (Thermo Fisher Scientific, Cat# D1306, RRID: AB_2629482) at 1:2000 to stain nuclei.

Images were acquired on a Nikon ECLIPSE Ti2 with Plan Apochromat VC 20x objective (N.A. = 0.75), and analysis was performed using Cell Counter of ImageJ (N.I.H., Bethesda, MD). Numbers of GFP-expressing OXT neurons (GFP^+OXT^+), GFP-expressing neurons without OXT immunostaining (GFP^+), and OXT neurons without GFP labeling (OXT^+) in the PVH were counted. The co-localization percentage of GFP-expressing OXT neurons (GFP^+OXT^+) in GFP-expressing neurons (GFP^+ + GFP^+OXT^+) and OXT-expressing neuron (OXT^+ + GFP^+OXT^+) represent specificity and efficiency of the sparse labeling strategy, respectively.

SINGLE-MOLECULE FLUORESCENT *IN SITU* HYBRIDIZATION, IMAGE ACQUISITION AND ANALYSIS

In situ hybridization was carried out according to published protocols, with minor modifications.[29] Hybridization chain reaction (HCR) probes targeting the coding sequence were designed using software from https://github.com/GradinaruLab/HCRprobe [87] and synthesized by Sangon Biotech, Shanghai, China. Briefly, brains were dissected, immersed in 4% PFA for 16 h, and then dehydrated with 20%–30% diethylpyrocarbonate (DEPC)-treated sucrose for 16 h. Tissues were then embedded in optimal cutting temperature (OCT) compound and cryosectioned at 30-40 μm. Sections were permeabilized in 70% ethanol for 16 h at 4°C, followed by 0.5% Triton X-100 in PBS at 37°C for 1 h, and treated with 10 μg/ml Protease K. After 3 washes with 2× sodium chloride sodium citrate containing Tween 20 (SSCT, 0.1% Tween-20 in 2× SSC) at room temperature, sections were pre-hybridized in 30% probe hybridization buffer (Molecular Instruments) for 10 min at 37°C and then incubated in 30% probe hybridization buffer containing HCR probes (10 μM each) at 37°C for 16 h. Sections were finally washed 3 times with 2× SSCT at 37°C. The HCR amplification steps were performed as previously described.[29] Images was acquired using a 20× objective on the Leica TCS SP8 confocal microscope and analyzed using Cell Counter in ImageJ.

SINGLE-CELL PROJECTOMES: DATA ACQUISITION AND ANALYSIS

fMOST image collection and preprocessing

Whole-brain images of sparse labeling samples were acquired using fluorescence micro-optical sectioning tomography (fMOST) technology. The raw image dataset of each sample includes two channels: the GFP channel (channel 1, CH1) contains morphological information of labeled neurons, while the propidium iodide (PI) channel (channel 2, CH2) contains cytoarchitectonic information. Each dataset has approximately 10000 raw images of 30000 × 20000 pixels of both CH1 and CH2, with a voxel resolution of 0.35 × 0.35 × 1.0 μm^3. The coordinate system of raw images is kept consistent in all subsequent processing. The X, Y and Z values of coordinates increased in value along the right-left (X), dorsal-ventral (Y) and anterior-posterior (Z) directions.

TB-sized CH1 raw images were divided into one million data cubes of 256 × 256 × 100 voxels using the FNT-slice2cube command of the Fast Neurite Tracer (FNT) software,[25] compressed using the high-efficiency video coding (HEVC) method for reconstruction. CH1 images were downsampled to a resolution of 20 × 20 × 20 μm^3 in the whole-brain projection overview to facilitate identification of the reconstruction start point.

Single-neuron reconstruction of axons, dendrites and somata

Single cell axonal projections were manually reconstructed from three sparsely and brightly labeled samples, aided by the FNT software.[25] Full axonal arbors of 115 neurons from sample 18696 (lactating female), 65 neurons from sample 195037 (virgin female) and 84 neurons from sample 195038 (virgin female) were traced. To ensure accurate reconstruction, all axonal arbors were traced by two independent experienced tracers (>3 months of tracing experience); reconstructed results were then merged and examined by another experienced tracer. A previous study, which used the same FNT software, examined tracing quality using quantitative measurements and showed that experienced tracers generated very similar reconstructions, and that accuracy was further increased by merging.[25] Tracing starting points were bright terminals outside of the PVH, to avoid bias in soma positioning; all brightly labeled neurons were traced. As shown in Videos S1 and S2, tracing was done using 0.35 × 0.35 × 1.0 μm^3 high resolution image datasets. The FNT software subdivided datasets into cubes (89.6 × 89.6 × 100 μm^3), and automatically loaded the next cube to be traced. At this resolution, axons can be easily distinguished from each other. Occasionally, when an axon tangled with another fiber near the soma,

we traced both fibers and usually resolved the issue; occasionally, tracing was abandoned because axons could not be traced back to the soma.

Labeled cells bodies in sample 195038 were sufficiently dispersed, allowing for dendrite reconstruction; the dendrites of all 84 neurons with traced axons were reconstructed using FNT. The somata of all neurons with traced axons were reconstructed, together with other brightly labeled somata in these samples (200, 175, 273 cells from sample 18696, 195037, 195038, respectively), using threshold segmentation algorithm and Amira software (ThermoFisher Scientific). Somata were automatically detected; when brightly labeled dendrites were detected as parts of soma, corrections were made. The proportion of traced projections, as a percentage of total somata analyzed, is as follows: 18% of PVHpv (2 reconstructed axons /11 reconstructed soma), 34% of PVHap (16/47), 36% of PVHmpd (134/376), 50% of PVHpml (78/156), 60% of PVHmm (32/53) and 40% of PVHpmm (2/5).

fMOST image registration to CCFv3

Features were extracted from the downsampled CH2 images at 10 × 10 × 10 μm^3 resolution for registration using Amira software. The selected features, as previously described,[88] include whole-brain outline, anterior commissure temporal limb (act), cerebellum outline, cc, CP, fasciculus retroflexus (fr), hippocampal region (HIP), MH, VIIn, mammillothalamic tract (mtt), PVH, PG, VL, V3, AQ and V4. These extracting features were mapped to the equivalent structures in CCFv3 to obtain accurate transformation parameters. Following alignment of sample brains to CCFv3 in 3D, the SWC files of soma centers, and reconstructed axons and dendrites were warped to CCFv3 brain space using the generated deformation fields.

To assess accuracy of registration, we overlaid the aligned boundary of CCFv3 brain structures to the downsampled CH2 images (10 × 10 × 10 μm^3) (Figure S1). Registration was mostly accurate, except for some areas surrounding the ventricle system and in basal ventral brain regions; the ventricles in our samples were larger than those of CCFv3, making alignment of small nuclei below V3 difficult; adding more features did not improve registration accuracy. ME-projections of C1 neurons were most affected by this issue; the projection strengths and terminals of C1 neurons mistakenly registered to PVp were reclassified to ME, to more accurately reflect the true projection of these neurons. Other registrations were sufficiently accurate for subsequent analyses.

Please note that the registration used in this study is slightly different from that of the website hosting our data. SWC files can be requested from the lead contact.

Hierarchical clustering of reconstructed OXT neurons based on single-neuron projectomes

Axons and dendrites were reconstructed in SWC file format. For quantification of axon projection patterns, SWC files were registered and resampled to CCFv3. CCFv3 contains 671 brain regions; for optimal visualization (Figure 2C), we merged sub-divisions of some brain regions and deleted regions without axon fibers. For example, MOp1 (primary motor area layer 1), MOp2/3, MOp5, MOp6a, MOp6b, MOs1 (secondary motor area layer 1), MOs2/3, MOs5, MOs6a and MOs6b were merged into MO (somatomotor areas); LSc (lateral septal nucleus caudal part), LSr (rostral part) and LSv (ventral part) were merged to LS. Brain regions were merged with the aim of showing CCFv3 ontology at the same level of classification. After merge and deletion, axonal fibers and terminals were distributed in 214 and 172 brain regions respectively; merged regions are listed in Table S3.

The total axon length of each reconstructed neuron in each brain region was defined as its projection strength (PS) in that brain region; all PS combined constituted the projectome of each neuron. The projectome of each reconstructed neuron as a vector was used to calculate the Canberra distance[89,90] between pairs of reconstructed neurons, to obtain the dissimilarity matrix. The Canberra distance d between vectors p and q in an n-dimensional real vector space is as follows:

$$d(p,q) = \sum_{i=1}^{n} \frac{|p_i - q_i|}{|p_i| + |q_i|}$$

where $p = (p_1, p_2, \ldots, p_n,)$ and $q = (q_1, q_2, \ldots, q_n,)$ are vectors.

Hierarchical clustering of the dissimilarity matrix was carried out using the Ward aggregation method, which minimized total within-cluster variance. The best number of clusters was determined using the R NbClust package,[26] which clusters results using different indices and proposes the best clustering scheme. For all reconstructed axons, based on the majority rule, an optimum of 2 clusters was selected by 10 indices among 20; for the C1 and C2 subtypes, the numbers are 3 clusters selected by 7 indices among 23, and 3 clusters selected by 13 indices among 22, respectively.

Correlation matrix of reconstructed axon projection strength and targets

To describe the co-projection relationship of reconstructed axons, we calculated the Spearman's rank coefficient of correlation between individual brain regions based on axon length and terminal number. The correlation matrix was hierarchically clustered using the Ward aggregation method (Figures 4O–4Q, 5O–5Q, and S3A–S3E; Tables S4, S5, S6, S7, and S8). Specializing insignificant correlation coefficients and wiping away from the corresponding glyphs were performed to emphasize the significant correlations.

Analysis of morphological features of individual neurons

We calculated soma morphological features, including soma center of homogeneous mass, volume, area and BoundingBoxOO (object-oriented) length (representing long axis), using Imaris (Oxford instruments). In addition to single-neuron projectomes, we

analyzed axon morphological features, including registered axon length, number of axon terminals and number of target regions. Dendrite morphological features analysis included number of primary dendrites, averaged length of primary dendrites and average terminal number of primary dendrites. The morphological character matrix composed of the above parameters, except for X coordinate of soma center. Dimensionality reduction of the morphological matrix was carried out using the Uniform Manifold Approximation and Projection (UMAP) method[91] for unsupervised dimension reduction, where each neuron was color-coded based on projectome clusters, subtypes or soma location.

Structure extraction of PVH and other brain regions

Because CCFv3 does not include PVH subdivisions, and the shape of PVH in Allen Reference Atlas version 2 (ARAv2) was sufficiently different from that of CCFv3, we manually delineated PVH subdivisions in CH2 image datasets at 10 × 10 × 10 μm^3 resolution in Amira, referencing the CH2 downsampled images at 1 × 1 × 10 μm^3 resolution as needed; the CH2 datasets at 1 × 1 × 10 μm^3 resolution was too big to load into Amira. We tried our best to match our subdivision delineation to both CCFv3 and ARAv2 outlines. In doing so, paraventricular hypothalamic nucleus, descending division, dorsal parvicellular part (PVHdp) and paraventricular hypothalamic nucleus, descending division, medial parvicellular part, ventral zone (PVHmpv) were combined into PVHmpd. For characterizing the morphological features of different clusters or subtypes reconstructed neurons, we first analyzed their soma, dendrite and axon parameters according to projectome clusters or subtypes. We then mapped somata and dendrites onto PVH subdivisions for further characterization.

To assay axons projecting near the ventricle system (Figures 6I–6K), a 50$\sqrt{2}$ μm zone[67] along the ventricle boundary was delineated. Unregistered reconstructed axons were used.

For 3D rendering of soma, dendrite and axon distributions (Figures 6E, 6F, and 7F), the whole-brain outline and the following regions structures, based on their unique gray value of the CCFv3, were extracted using Amira: RE, Xi, PVH, ME, MEA, BST, SO, PVa, PVi, ARH, PD, PVpo, SBPV, VLPO, PVHd, LHA and TU.

MESOSCALE PROJECTOMES: DATA ACQUISITION AND ANALYSIS

fMOST image collection and preprocessing of bulk labeled samples

We used fMOST technology[23,24] to collect images of 11 bulk labeled samples, including 3 virgin female (16192, 16247 and 16248), 4 lactating female (16266, 16265, 16500 and 16267) and 4 male mice (16246, 16455, 16454 and 16456). Each dataset contained 5000 raw images of two channels at 0.32 × 0.32 × 2.0 μm^3 resolution (30000 × 20000 × 2 voxels). CH2 raw images were maximally projected in Z and downsampled to a resolution of 3.2 × 3.2 × 50 μm^3 for later analysis. 3 mice were analyzed for all conditions. Quantification was made in the hemisphere without SO labeling. The 4th sample was substituted in when a sample had missing features.

Mesoscale projection intensity in bulk labeling datasets

The analysis of axon distribution in bulk labeling samples was performed earlier in this study, when less sophisticated registration was available. To ensure the accuracy of brain region boundary and precise analysis, we manually extracted the following brain regions in downsampled CH2 datasets (3.2 × 3.2 × 50 μm^3): MOB, AON, mPFC (ACA + PL + ILA), ORB, Ins [AI + GU (gustatory areas) + VISC (visceral area)], CP, ACB, GPe, GPi, SNc, SNr, VTA, MS, NDB + SI + MA, LSX [LS + SF + SH (septohippocampal nucleus)], BST, HIP, LA, BLA, CEA, MEA, MH, PVT, VMH, LHA, SO, SCH, ZI, ME, SC [SCs (superior colliculus sensory related) + SCm], PAG, DR, LC, PB, NTS and IRN. Extraction of brain regions was performed using Adobe Photoshop CC 2016 (Adobe Inc.). We loaded single images containing above mentioned regions from the CH2 3.2 × 3.2 × 50 μm^3 image dataset. Then, the template image of ARAv2 was scaled, rotated and translated to match the regions around the extracted region of loaded image, as much as possible, using the Puppet Warp tool and other transformation features in Photoshop. The boundary of extracted regions was delineated based on the mapped template image of ARAv2. The extracted regions of interest (ROI) was saved as single binary mask image for subsequent analysis. If a section contained multiple brain regions, separate ROIs were extracted.

CH1 raw images at original resolution were analyzed using the extracted ROIs, using Matlab (MathWorks Inc.). The total pixel number and ROI area of each brain region (BR) was used to quantify mesoscale projection intensity (MPI), defined as:

$$\mathrm{MPI} = \frac{\sum_{i=1}^{n} Signal\ (BR)}{\sum_{i=1}^{n} Area\ (BR)} \Big/ \frac{\sum_{i=1}^{n} Signal\ (PVH)}{\sum_{i=1}^{n} Area\ (PVH)}$$

For analysis of the correlation between sparse and bulk labeled samples (Figure S6C), whole-brain mesoscale projection intensity of one bulk labeled sample (16454) was quantified. Downsampled coronal sections (2 × 2 × 2 μm^3) were registered to CCFv3; registration was manually checked for accuracy. Fluorescent signals of labeled OXT fibers in registered coronal sections were segmented using the modified maximum entropy threshold segmentation algorithm. MPI of 16454 was defined as total signal (pixels) of each brain region divided by its volume (voxels). Single-neuron projection intensity (snPI) was defined as projection strength (μm) of

each brain region divided by its volume (μm^3). For correlation calculation, MPI of each brain region was quantified as $\ln(MPI \times 10^7 + 1)$ and snPI of same region was quantified as $\ln(snPI \times 10^7 + 1)$.

QUANTIFICATION AND STATISTICAL ANALYSIS

Animals were not randomized. Statistical analysis of morphological parameters was performed using GraphPad Prism 8 (GraphPad Software, La Jolla, CA, USA). No statistical methods were used to predetermine sample sizes. Data are presented as mean ± SEM. Gaussian distribution of the data was assessed using the Anderson-Darling test, Shapiro-Wilk normality test, Kolmogorov-Smirnov test or D'Agostino & Pearson normality test. If the data pass one of the Gaussian distribution tests, parametric tests (unpaired t-test for two groups or one-way ANOVA with Tukey's post hoc test for three or more groups) were used, otherwise nonparametric tests (Mann-Whitney and Kolmogorov-Smirnov for unpaired two groups, and Kruskal-Wallis test with Dunn's post hoc test for three or more groups) were used. For experiments with two independent variables, two-way ANOVA followed by Bonferroni's multiple comparisons test was used. Correlations were assayed using simple linear regression and Spearman's rank correlation coefficient.